The Interaction Between Two 2D Rarefied Vapor Jets

T.J.M. Broeders

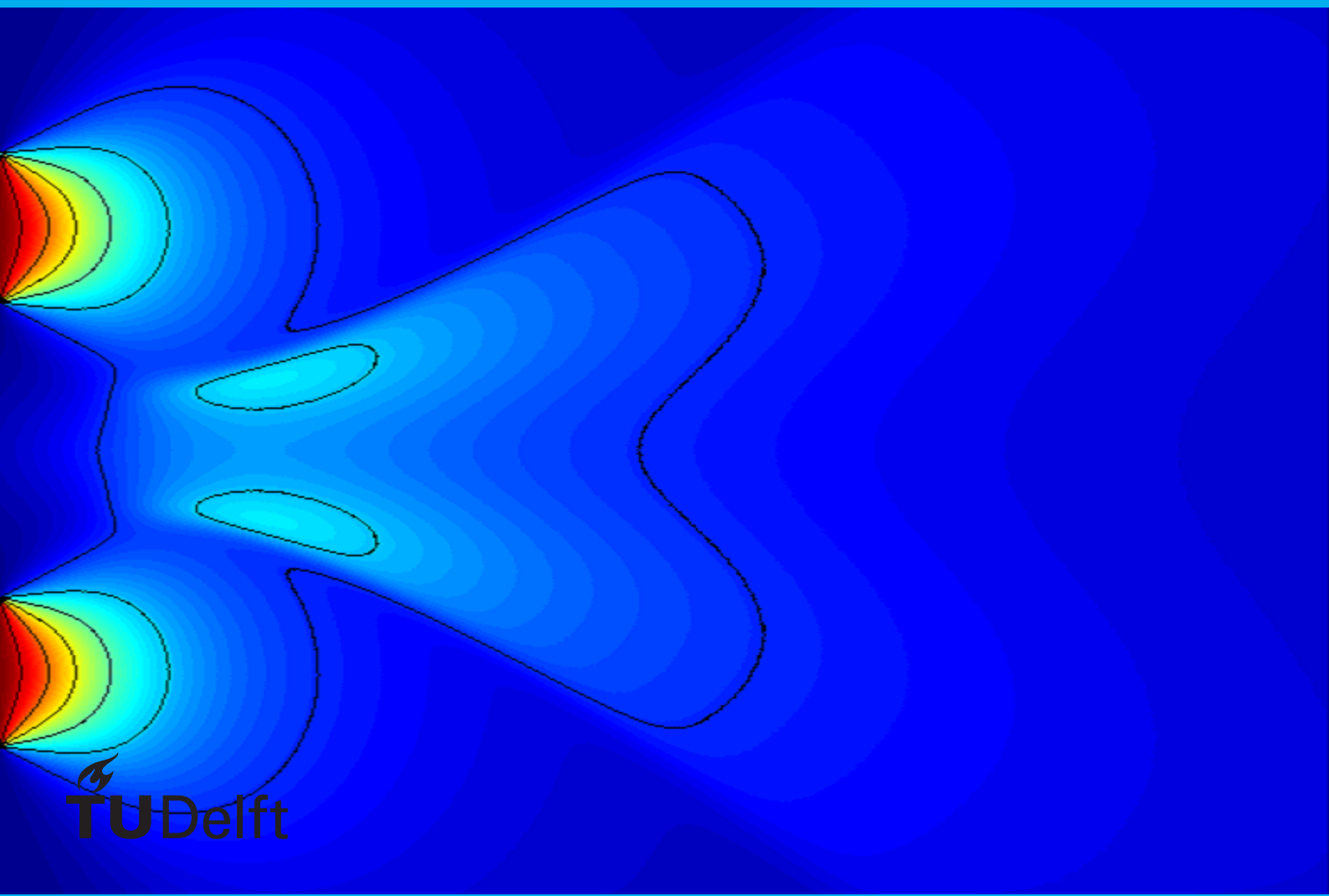

TU Delft

THE INTERACTION BETWEEN TWO 2D RAREFIED VAPOR JETS

by

T.J.M. Broeders

in partial fulfillment of the requirements for the degree of
Bachelor of Science
Applied Mathematics and Applied Physics
at the Delft University of Technology,
to be defended publicly on Tuesday April 9, 2019 at 15:00 PM.

Student number:	4174879
Project duration:	Oct 15, 2018 – Apr 9, 2019
Supervisor:	Prof. dr. ir. C.R. Kleijn
	Dr. ir. F.J. Vermolen
	E. Vesper, M.Sc.
Thesis committee:	Dr. J.L.A. Dubbeldam
	Dr. S. Kenjereš

TU Delft

ABSTRACT

Steel is commonly coated to protect it from corrosion. One method of applying this is by using Physical Vapor Deposition, which can be done by using multiple jets. In this process jets next to each other interact. This paper's main aim is to investigate the interaction effect of two rarefied two-dimensional vapor jets in vacuum and how this is influenced by the distance between jets and inlet density. Furthermore, the analytical solution for the collisionless case for a single jet is extended to dual jets. Additionally, the objective is to maximize the processing speed for the use of coating, with a certain uniformity for the parameters researched in this paper and finding an optimal method in doing so. This study is done by using the Direct Simulation Monte Carlo (DSMC) method.

The analytical solution gave the same results as the collisionless DSMC method for both single and dual jets. Simulations with a strong interaction effect resulted in a shock. These behaved similar compared to three-dimensional jets, in the plane of the jets. The shock results in a secondary jet, which has a lower density in the middle. The interaction effect depends primarily on the inlet density. Multiple regimes are observed for different inlet density ranging from small change in properties to a shock wave, with a transitional regime inbetween. The influence of the distance between the jets is found to result in a higher density at the axis of the inlet behind the shock, for bigger distance between jets. However, for very small distances between jets compared to the inlet size the shock is weak. For the optimization, it resulted in the conclusion that the optimal coating in general is applied with the smallest distance between jets. This generally gives a better uniform coating and increased performance. However, this is not always the case when constraining the distance between the jets and sheet, as it only holds if the shock between the jets for this distance. Furthermore, an approximation is found for the optimization, which results in fewer simulations needed.

CONTENTS

1

INTRODUCTION

One of the greatest threats to metal is corrosion. One way to protect the metal is by coating it with Zinc. Steel is commonly coated by immersing it in a bath of molten zinc known as hot dip galvanization[1]. However, this reheats the steel, which is not always preferred. Another option for applying a coating is using Physical Vapor Deposition[11]. In this process zinc vapor is sprayed on the sheet, after which it attached on contact. The process speed of this method depends partly on the number of vapor jets used. However, two close jets can interact with each other. This interaction changes the vapor deposition profile and can even result into a shock. This shock results in irregular coating, which could lead to problems further in the process line. Therefore, a coating is preferable applied uniform and thus, understanding the interaction effect of two vapor jets could help optimize this coating process. The interaction effect of two three-dimensional jets has been researched before[9][7][6][4]. However, there is little literature on the interaction effect for the two-dimensional case, which represents two infinite long slits in three dimensions.

The aim of this study is to investigate the interaction effect of two rarefied vapor jets in two-dimensions and how to optimize its vapor deposition. This is done by doing simulation using the Direct Simulations Monte Carlo (DSMC) method. However, this is a computational costly method for which simulations can take up to two weeks. Therefore, we start by first reviewing the analytical solution for the collisionless case for a single two-dimensional jet[3] and expanding it to the dual jets, as this could serve as a useful comparison, which is not as computational costly. Additionally, it gives the solution for one utmost extreme. After this, the conditions at which a shock occurs is studied. The interaction effect is then compared for different inlet densities and distances between jets. The inlet density is expected to play a major role in the interaction effect, as this defines the gas flow characteristics. The density greatly influences the collision frequency, which in turn causes the particles to interact more. The distance between the inlets is expected to have a smaller influence on the interaction effect for most cases, but it could influence the deposition profile. For the last part, this thesis will examine a method for optimizing the process conditions to obtain the desired vapor deposition profile, which

is a fast vapor deposition under the condition that the coating is applied within a certain uniformity.

2

THEORY

2.1. KINETIC THEORY OF GASES

The kinetic theory describes a gas as a system containing a large number of small particles (molecules). These particles behave according to classical mechanics. As in most gases, it is assumed that the average distance separating the particles is large compared to their size, therefore interaction involving three or more particles can be neglected and thus only binary collisions are taken into account. In this section, we explain the phase density function and how it is used in kinetic theory of gases to calculate the gas flow properties and how the analytical solution for the collisionless case is derived.

2.1.1. PHASE DENSITY FUNCTION

In kinetic theory gas flow depends on a huge number of particles, which is practically impossible to keep track of individually. A solution for this is by using a phase density function $f\left(x, y, z, v_x, v_y, v_z, t\right)$. Here x, y and z stand for the coordinates of the position and the values v_x, v_y and v_z represents the velocity of a particle in corresponding directions, which is also represented by the velocity vector $\boldsymbol{v}$. This function represents the relative chance to find a particle at position $\boldsymbol{r}$ with velocity $\boldsymbol{v}$. The velocity distribution for each point is thus contained in f. The phase density function can therefore be used to calculate the macroscopic properties of the gas. The local values for number density n, average velocity $\boldsymbol{V}$ and temperature T are calculated by[2]

$$n = \iiint_{\mathbb{R}^3} f \, \mathrm{d}\boldsymbol{v}, \tag{2.1a}$$

$$\boldsymbol{V} = \frac{1}{n} \iiint_{\mathbb{R}^3} \boldsymbol{v} f \, \mathrm{d}\boldsymbol{v}, \tag{2.1b}$$

$$T = \frac{m}{3nk} \iiint_{\mathbb{R}^3} ||\boldsymbol{V} - \boldsymbol{v}||^2 f \, \mathrm{d}\boldsymbol{v}. \tag{2.1c}$$

In the equation for the temperature, k stands for the Bolzmann constant and m represent the mass of a molecule.

2.1.2. BOLTZMANN EQUATION

In the previous part we explained the phase density function f. This function changes over time as particles move and collide with each other. In 1872[15], Ludwig Boltzmann established a partial differential equation describing the progression of the density function. This equation, known as the Boltzmann equation, shows that the change in time can be split into two parts. They are the change caused by collisions and the change caused by movement $\boldsymbol{v}$ and acceleration due to an external force $\boldsymbol{F}$, i.e.

$$\frac{\partial f}{\partial t} + \boldsymbol{v} \cdot \frac{\partial f}{\partial \boldsymbol{r}} + \frac{1}{m}\boldsymbol{F} \cdot \frac{\partial f}{\partial \boldsymbol{v}} = \left(\frac{\partial f}{\partial t}\right)_{coll}, \tag{2.2}$$

where $\boldsymbol{r}$ stands for the point in space. The collision term was also determined by Boltzmann. The Boltzmann equation has for most cases no known exact solution and is therefore commonly solved with a numerical approach. In this paper the Direct Simulation Monte Carlo (DSMC) method is used to evaluate the particle behavior.
The phase density function for a gas in thermodynamic equilibrium is expressed by the Maxwell-Boltzmann distribution[14], i.e.

$$f\left(v_x, v_y, v_z\right) = n\left(\frac{m}{2\pi kT}\right)^{3/2} \exp\left(-\frac{m||\boldsymbol{v}||^2}{2kT}\right). \tag{2.3}$$

This equation is independent of the position and is the time independent solution for the Boltzmann equation for a closed box. When taking stream velocity $\boldsymbol{V}$ into account, the velocity $\boldsymbol{v}$ is replaced by $\boldsymbol{v} - \boldsymbol{V}$. The Maxwell-Boltzmann distribution described above is for a three dimensional gas, and is proportional to a three dimensional normal distribution. This has the property that the velocities v_x, v_y and v_z are uncorrelated. Therefore, the equation can be written as

$$f = n\, f_x\, f_y\, f_z, \tag{2.4}$$

with the functions f_x, f_y and f_z as one dimensional normal distributions, i.e.

$$f_x = \sqrt{\frac{m}{2\pi kT}} \exp\left(-\frac{m|v_x - V_x|^2}{2kT}\right). \tag{2.5}$$

These functions have the property, $\int_{-\infty}^{\infty} f_x \,\mathrm{d}x = 1$. These distributions are used in calculating the analytical solution for the collisionless case and for initializing the particle speed in the simulation.

2.1.3. COLLISIONLESS ANALYTICAL SOLUTION

As mentioned in previous section, the Boltzmann equation is not commonly solved analytically. However, there is an analytical solution for the gas flow of a single jet expansion in vacuum if collisions are ignored. The analytical solution for the number density and velocity were solved by Cai [3], who used Narasimha's[12] work for collisionless expansion from a point source.
We assume a vacuum space without external forces and introduce a point source of molecules at the origin. All particles in the domain come from the source. The velocity of each particle is constant, as it is not changed by collisions or external forces. This means that at a point $\boldsymbol{r}$, there are only particles with velocity $\boldsymbol{v}$ which points into the

same direction, i.e $\hat{\boldsymbol{r}} = \hat{\boldsymbol{v}}$. This is equivalent to $\boldsymbol{v}t = \boldsymbol{r}$ for some positive value of t.
For a two-dimensional jet in vacuum emanating from a finite-size slit, the previous principle still holds. Every particle comes from a point on the inlet. Therefore, the condition $t\boldsymbol{v} = \boldsymbol{r} - \boldsymbol{r}_s$ must hold for some positive value t and some coordinate $\boldsymbol{r}_s$ of a point on the slit. In other words, at point $\boldsymbol{r}$ only particles for which the conditions hold, are found. Therefore, define the set $\Omega_{\boldsymbol{r}}$ as the collection of all the velocities $\boldsymbol{v}$ for which the condition holds. This set is position dependent and each velocity in this set corresponds to a point of the slit. At the entire inlet is assumed to have the Maxwell-Boltzmann distribution as phase density function f_0. The phase density function for a point $\boldsymbol{r}$ can then be expressed by

$$f(\boldsymbol{r}, \boldsymbol{v}) = \begin{cases} f_0(\boldsymbol{v}) & \boldsymbol{v} \in \Omega_{\boldsymbol{r}}, \\ 0 & \boldsymbol{v} \notin \Omega_{\boldsymbol{r}}. \end{cases} \tag{2.6}$$

Using this, the equations 2.1a-2.1c can be written as the integral over the set $\Omega_{\boldsymbol{r}}$. The macroscopic gas properties can be written as:

$$n(x,y) = \iiint_{\Omega_r} f_0 \, \mathrm{d}\boldsymbol{v}, \tag{2.7a}$$

$$\boldsymbol{V}(x,y) = \frac{1}{n(x,y)} \iiint_{\Omega_r} \boldsymbol{v} f_0 \, \mathrm{d}\boldsymbol{v}, \tag{2.7b}$$

$$T(x,y) = \frac{m}{3kn(x,y)} \iiint_{\Omega_r} ||\boldsymbol{V} - \boldsymbol{v}||^2 f_0 \, \mathrm{d}\boldsymbol{v}. \tag{2.7c}$$

The equations for number density and velocity where solved and validated by Chumpei and Boyd[3]. The temperature was solved and validated by Khasawneh, Liu and Cai[8]. These solutions can be found in appendix A.

2.2. THE KNUDSEN NUMBER

In rarefied gas flow particle behavior results from collision. Therefore, the frequency of collisions influences the gas behavior. A gas can be characterized by the Knudsen number Kn. This number is a dimensionless number defined by the ratio between the mean free path λ and a characteristic length L, i.e.

$$Kn = \frac{\lambda}{L}. \tag{2.8}$$

The mean free path is the average distance particle move between collisions. The length L is in literature loosely defined as a characteristic length to some traits of a system. In this paper, the following definitions for Knudsen numbers are used.

2.2.1. THE STAGNATION KNUDSEN NUMBER

Each of the simulations depends on its inlet parameters. In practical experiments, these parameters depend on how the gas is inserted. For the vapor deposition apparatus we study, this is done by evaporating a material in a box. The gas is then assumed to leave the box accelerating in an isotropic process from stagnation conditions up to the speed

of sound. The mean free path λ_s at the stagnation condition is then used for the stagnation Knudsen number, denoted by

$$Kn_s = \frac{\lambda_s}{h}. \tag{2.9}$$

Here h stands for the width of the inlet.
In this paper, the same value for h is chosen for all cases. Furthermore, the inlet temperature T_0 and velocity $\boldsymbol{V}_0$ are also kept the same. The inlet number density n_0 is changed and depends on Kn_s by equation[9]

$$Kn_s = \frac{1}{\sqrt{2}\sigma\, n\, h}, \tag{2.10}$$

with collision cross-section σ.

2.2.2. THE PENETRATION KNUDSEN NUMBER

The degree of interaction of two vapor jets can be classified by the penetration Knudsen number Kn_p. This was introduced by Dankert and Koppenwallner [9] to distinguish between regimes.

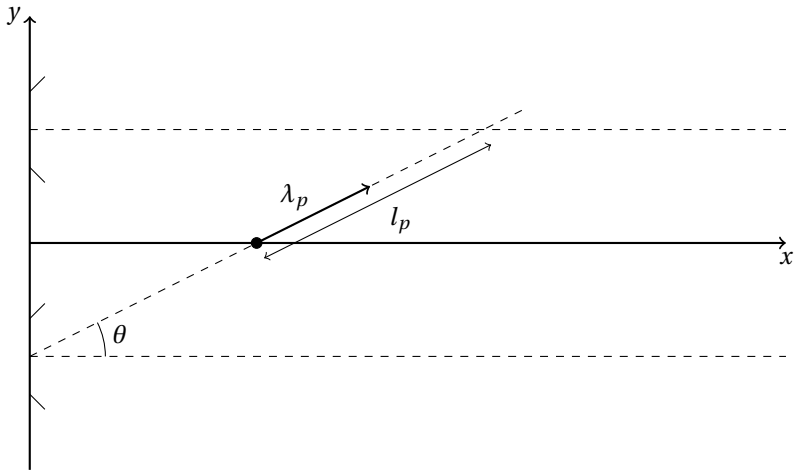

Figure 2.1: Defining Kn_p for dual jets, showing the penetration mean free path λ_p, the penetration length l_p and the angle θ from the inlet.

The penetration Knudsen number is only defined on the mid-line between the jets. Looking at figure 2.1, the particles on the mid-line coming from the bottom inlet with angle θ, start to move through the other plume. The distance it needs to travel to move past middle of the other plume is denoted by l_p. The penetration mean free path λ_p, is defined as the average distance a particle from one plume travels before it collides with a particle from the other plume. The penetration Knudsen number is defined by the ratio between λ_p and l_p, i.e.

$$Kn_p = \frac{\lambda_p}{l_p}. \tag{2.11}$$

This Knudsen number depends on the angle θ, but can also be expressed depending on the position of the mid-line. In practice, particles could have collided many times before arriving at the mid-line. Therefore, this number is calculated without the interaction taken into account.
Equation 2.11 can be solved by using the data of a single jet. The mean free path λ_p of a particle going through one jet can be approximated by assuming that the relative speed between two plumes is equal to $2V_y$. The gives us

$$\lambda_p = \frac{||\boldsymbol{V}||}{2V_y n\sigma}, \tag{2.12}$$

with collision cross-section σ. Using this equation with equality $\frac{||\boldsymbol{V}||}{L} = \frac{V_x}{l_{p,x}}$, the equation can be written as

$$Kn_p = \frac{1}{2n\sigma l}. \tag{2.13}$$

Kn_p depends on the position. Therefore, it is the minimum value $Kn_{p,min}$ used to describe the interaction effect.

2.3. DIRECT SIMULATION MONTE CARLO

The Direct Simulation Monte Carlo (DSMC) method is commonly used to simulate rarefied gas flow [5, 10]. It is part of computational fluid dynamics (CFD) and it is a probabilistic simulation for solving the Boltzmann equation. DSMC is a particle based method which uses a stochastic model to determine collisions to mimic gas flow. The movement and collision of particles are decoupled from each other. This makes it computationally faster than other particle based simulations such as Molecular Dynamics (MD). However, this also makes it inaccurate for cases in which the exact collision plays a major role. In this section we shall explain the workings of the DSMC method and how to get accurate results.

2.3.1. THE DSMC METHOD

In DSMC, particles representing a large number of molecules are used to simulate gas flow. The workings of DSMC can be summarized by a few simple steps. These steps are conducted each time step of the DSMC simulation. The computational domain is discretized on a mesh. First initialize particles with a prescribed spatial and velocity distribution at the inlet, then move the particles during a time step Δt. After that, particles within the same mesh cell are selected as potential collision partners, after which collisions are computed. The mesh is then used to sample the properties as the last step.
We shall discuss these steps in more detail. At the inlet boundary new particles are initialized. These particles velocities and positions are sampled from their corresponding distribution. For the position this is a uniform distribution and for the velocity this is the Maxwell-Boltzmann distribution 2.3. After this, each particle is moved depending only on its own velocity, and thus independent of other particles. Particles moving over the boundary are dealt with according to the type of boundary. Subsequently, the collisions are calculated. Particles are first sorted by cell. For each cell the maximum number of collisions is determined. This is achieved by first determining the maximum number of

collisions. For each of these collisions, two random particles are chosen in the cell. Each of these pairs are then accepted or declined to collide randomly depending on their relative velocity. Each accepted collision changes the velocities of the two particles. The new velocities satisfy the momentum and energy conservation and are determined by the collisions angle which is chosen by a stochastic process. There are different models[2] to simulate the collisions, such as the hard-sphere and soft-sphere model. In this paper, the variable hard-sphere model is used[2].
To conclude, here are some properties for a better understanding: The DSMC method does not take other particles into account when moving. It is possible to have two particles at the same position, and as the collision process in a cell does not take position into account, these particles have a normal chance to collide.

2.3.2. DISCRETIZATION ERROR

A DSMC simulation is always numerically stable, regardless of time-step, but not always accurate. The discretization error depends on the time step, the cell size and the number of particles per cell.
The time step Δt should be small enough for the particle to move multiple time steps between collisions, because the movement and collision process should be decoupled. In other words, Δt must be significantly smaller than the mean collision time τ_c. A good rule of thumb [2] is to set the time step smaller than one tenth of the mean collision time.
The cell size Δx should be small enough in order to avoid collisions of particles far apart from each other to prevent instant transport of energy and momentum over a large distance. Therefore, the cell size should be smaller than the mean free path λ. Bird [2] states that as a rule of thumb, the cell size should be smaller than one third of the mean free path.
The number of particles in a cell N_{cell} determines the number of possible different collisions. This should be sufficiently high such that two particles do not collide too often which each other and should also be sufficiently high to accurately calculate average gas properties. The rule of thumb[2] is that it should be above or equal to twenty.
In short, the criteria for an accurate DSMC simulation are:

1. $\Delta t < \frac{1}{10}\tau_c$,
2. $\Delta x < \frac{1}{3}\lambda$,
3. $N_{cell} \geq 20$.

Fulfilling these criteria throughout the domain results in high computational cost, especially for an expansion flow. Therefore, the criteria are fulfilled within and upstream the region of interest. In this paper, $\Delta t < \frac{1}{5}\tau_c$ is used to save computational time.
Particles should not be able to jump over cells. This commonly does not happen when following the rule of thumb above because a particle will be in a cell for around three time steps on average. However, particles can pass cells in cases with $\Delta x << \lambda$. This happens for example by disabling the collisions. In these cases, the flow velocity $\boldsymbol{V}$ should be taken into account such that on average the particles stay in the cell for two time steps, i.e. $\frac{||\boldsymbol{V}||\Delta t}{\Delta x} < 0.5$. Otherwise, a biased could be introduced as the probability for certain velocity could be effected.

2.3.3. AVERAGING MACROSCOPIC PROPERTIES AND THEIR STATISTICAL ERROR

There are different definitions for calculating the average of macroscopic properties. Those of the gases are determined for each separate cell. As we assume we have a steady state, an average can be obtained by using a number of time steps I_t. The number of particles in a cell N_{cell} can be averaged, with the average number of particles N_{av} in a cell defined by

$$N_{av} = \langle N_{cell} \rangle. \tag{2.14}$$

From this follows the density ρ, with the help of the number of molecules each particle represents n_{eqv}, the mass of single Zinc molecule m and the volume of the cell V_{cell}. The density can be calculated by

$$\rho = N_{av} \frac{n_{eqv} m}{V_{cell}}. \tag{2.15}$$

The average velocity of the gas in the cell U is calculated not by averaging over time but by averaging over the total number of particles N. This way, each particle is weighted by its number of time steps in the cell. The average velocity is the average of the particle velocities in the cell,

$$\boldsymbol{U} = \frac{1}{N} \sum_{i=1}^{N} \boldsymbol{v}_i. \tag{2.16}$$

The temperature T of the cell is calculated in a similar way, but as it is proportional to the variance of the velocity, it is calculated by the unbiased estimation of the variance, this gives

$$T = \frac{2m}{3k} \frac{1}{N-1} \sum_{i=1}^{N} |\boldsymbol{v_i} - \boldsymbol{V}|^2. \tag{2.17}$$

The version of dsmcFoam used, calculated T as

$$T = \frac{2m}{3k} \frac{1}{N} \sum_{i=1}^{N} |\boldsymbol{v_i} - \boldsymbol{V}|^2. \tag{2.18}$$

This formula is biased for small values of N[16] and should not be used in those cases.
The above discussed properties have a statistical error resulting from averaging over a finite number. These are explained by Sun and Boyd [16], and can be expressed as follows:

$$E_{N_{av}} = \sqrt{N} I_t, \tag{2.19a}$$

$$E_{\rho} = E_{N_{av}} \frac{n_{eqv} m}{V_{cell}}, \tag{2.19b}$$

$$E_U = \sqrt{\frac{kT}{mN}}, \tag{2.19c}$$

$$E_T = \sqrt{\frac{2T^2}{3N-1}}. \tag{2.19d}$$

These statistical errors do not take into account that particles stay in the cell for multiple time steps. A more accurate error estimate is discussed later in this paper. All of these

errors are proportional to $1/\sqrt{N}$, which can be increased by averaging over a longer time or by increasing the number of particles.

3

CASE SETUP

The DSMC simulation is conducted with OpenFoam+ solver of OpenFOAM-2.4.0-MNF[17]. The version used has a small bias in the calculations for the temperature, which is explained in section 2.3.2. The DSMC method implemented in OpenFoam uses subcells to separate the particles for the collision process. This method[2] divides each cell into eight smaller cells, in which particles have a higher chance to collide within the same subcell. Therefore, the length of cells is taken twice as large as the one given by the rule of thumb, explained in section 2.3.2. Furthermore, the time step has also been taken larger than the rule of thumb to increase computation time. The effect of the increased time step has been tested for a dual jets case, which gave no significant difference. The conditions set for the simulations in this paper follow

1. $\Delta t < \frac{1}{5}\tau_c$,
2. $\Delta x < \frac{2}{3}\lambda$ and
3. $N_{cell} \geq 20$

for all cells, except for the low density area at the boundary. For all simulations, the following inlet conditions are kept the same. The inlet velocity $\boldsymbol{V}$ is kept at 356.5m/s in the x-direction and the inlet Temperature T_0 at 600K. The simulations are done for the monatomic gas zinc. The collision follow the variable-hard sphere model. [2]
For the cases of the single jet flow, the domain is represented by figure 3.1. The width h of the inlet is 3.0mm for all cases. The size of the domain is $L_x = 75$mm by $L_y = 33$mm by $L_z = 0.001$mm, for which the length in the z-direction does not influence the results of the DSMC. The boundary conditions of the domain are deletion boundaries at the edges of the x,y-directions and a symmetry boundary in the z-direction, reducing the three-dimensional simulation to a two-dimensional case.

Figure 3.1: Representation of the solo jet expansion domain.

For the case of the dual jet expansion, the domain is shown by figure 3.2. In these cases most simulations have a size of $L_x = 30$mm by $L_y = l + 4.5$mm by $L_z = 0.001$mm, here the domain depends on the distance l to the middle of the inlet. The boundary conditions is the same as for the solo jet case except for the symmetry boundary at $y = 0$.

Figure 3.2: Representation of the dual jets expansion domain.

When particles pass through a symmetry boundary, their velocity is mirrored. Passing any other boundary results in the particle being deleted. This includes the inlet boundary boundary at which the particles are generated. This should give a difference between DSMC and experimental results, which should be taken into account when comparing. However, this is not part of the present study.

3.1. AUTOCORRELATION

As explained in section 2.3.3, the estimates for the statistical error do not take the effects of autocorrelation into account. This can result from particles being sampled multiple times. Decreasing the time step by half, doubles the number of particles N_{av} in equation 2.19b, but should not significantly decrease the observed statistical error. When particles are in a cell they can collide, however these collisions do not change the number of particles in the cell or the total momentum in the cell, as collisions follow the law of conservation of mass and momentum. This means that the velocity of the gas flow is also kept the same and such also the kinetic energy of the gas. It follows from energy conser-

vation, that the temperature is unaffected by collision. In short, the properties change only when particles enter or leave the cell. However, this is influenced partly by collisions, as they do exchange energy and momentum between particles. The autocorrelation is calculated for different points in the domain for 16000 time steps. Figures 3.3-3.6 shows the autocorrelation function, ACF, for $Kn_s = 0.0020$ for the point ($x = 0.293$mm, $y = 4.515$mm). This point is located 0.293mm behind the inlet, with the middle of the inlet at $l = 4.5$mm.

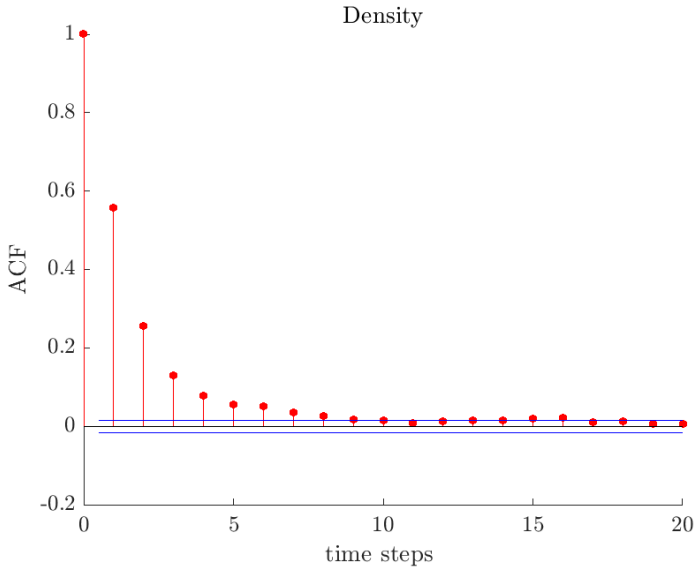

Figure 3.3: The autocorrelation function for the density at the point ($x = 0.293$mm, $y = 4.515$mm). The two lines represent the 2σ relative standard deviation of the density.

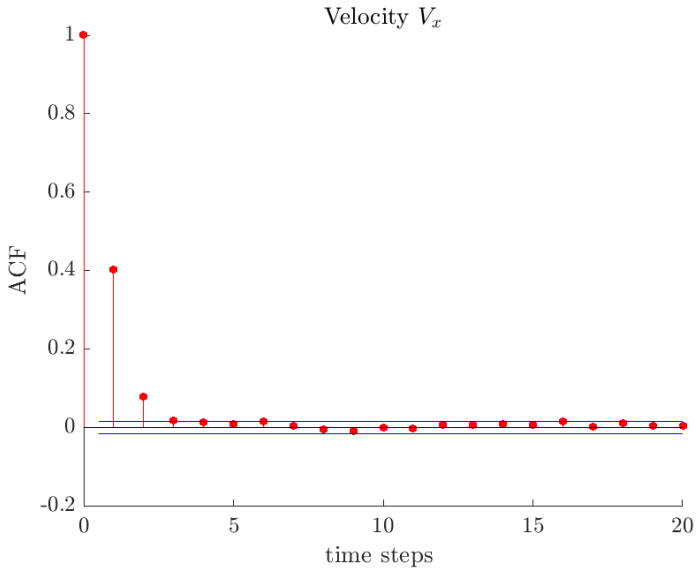

Figure 3.4: The autocorrelation function for the velocity V_x at the point ($x = 0.293$mm, $y = 4.515$mm). The two lines represent the 2σ relative standard deviation of the data.

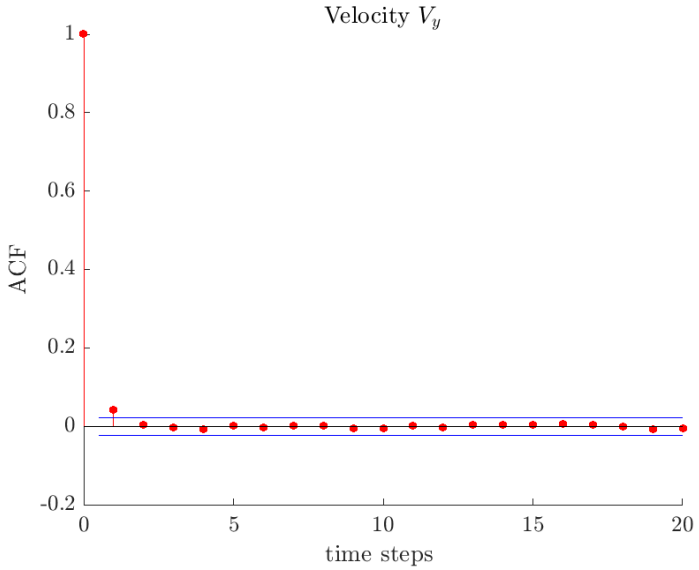

Figure 3.5: The autocorrelation function for the velocity V_y at the point ($x = 0.293$mm, $y = 4.515$mm). The two lines represent the 2σ relative standard deviation of the data.

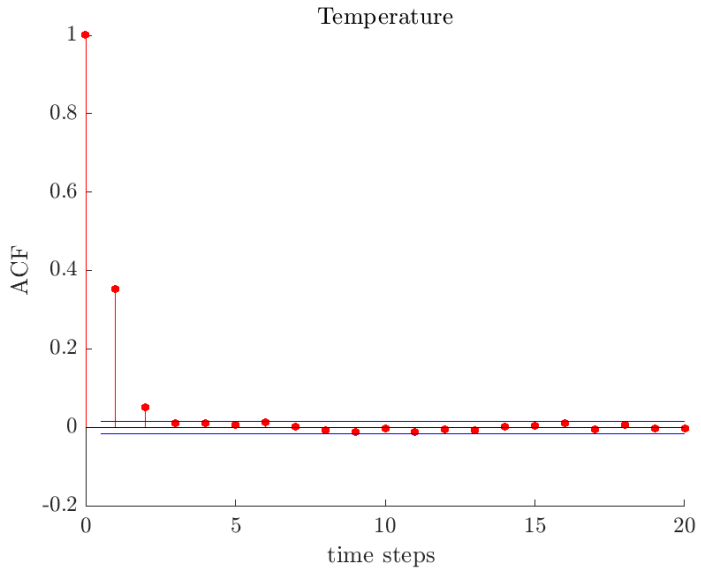

Figure 3.6: The autocorrelation function for the temperature at the point (x = 0.293mm, y = 4.515mm). The two lines represent the 2σ relative standard deviation of the temperature.

The figures shows that the auto correlation functions differ for different macroscopic properties. The density has a longer autocorrelation time compared to the others. This can be explained by the fact that the number density depends on the number of particles in the cell N_{cell}. This number can only change when particles enter or leave the cell by a set amount. The value of N_{cell} has, therefore, a higher chance to have a value close to previous value of N_{cell}. The other properties do not depend on a set amount. When the same number of particles would enter and leave, the number density is unchanged, but the other properties can be changed. Furthermore, individual properties of particles are changed by collisions.
The autocorrelation function shows that after a certain number of time steps the values are uncorrelated. However, this number does not represent the average, as it includes even the time-steps with small but noticeable autocorrelation. Using this number of time step gives thus an overestimation. Therefore, the difference between the first two points is used to calculate the average number of time steps τ needed. This is done by assuming the autocorrelation decreases by the same relative amount each time step. This method correlates better when comparing the expected error with the error found. Table 3.1 shows the average time steps τ for the different macroscopic properties at different points. It shows that larger cells have in general a larger value for τ. This is expected, as particles will be on average longer in these cells. However, this is not the only cause, as the diversity of the properties of the particles also influences the value of τ, which is lower for cells farther away of the inlet. The values for τ can be used to get a better error estimate by increasing the unautocorrelated errors in section 2.3.3 by its corresponding $\sqrt{\tau}$.
The values for τ found in table 3.1 are case depended. However, by keeping the same

Table 3.1: The number of time steps τ needed for significant unautocorrelated macroscopic property at different point, with corresponding cell size.

No.	position (mm)		cellsize (µm)		τ_ρ	τ_{V_x}	τ_{V_y}	τ_T
	x	y	dx	dy				
1	0.020	4.49	29.8	30.0	2.12	1.28	1.25	1.30
2	0.293	4.49	31.8	30.0	2.24	1.68	1.02	1.55
3	0.293	4.52	31.8	30.0	2.27	1.67	1.04	1.55
4	6.27	1.67	79.5	30.0	3.44	2.92	1.00	2.56
5	8.59	4.49	98.0	30.0	4.06	3.82	2.31	3.49
6	25.6	4.49	235	30.0	5.53	5.32	3.41	4.75
7	25.6	7.47	235	44.3	6.10	5.89	4.35	5.35

ratio between the cell sizes and the time step, we expect the values for τ to be roughly the same.

4

Analytic Solution for the Collisionless Case

The collisionless case can be solved analytically. We first compare the analytical solution for the single jet with DSMC results for a verification of the code. Additionally, we will show how collisions change the flow field of a single jet. After that, the analytical solution for the dual jets is derived from the single jet and compared to the DSMC.

4.1. Single Jet in Vacuum

For the single jet expansion in vacuum, the analytical solution for the collisionless case is compared with a collisionless DSMC simulation. The analytical solutions for the collisionless single jet expansion in vacuum are found in Appendix A. As shown in figures 4.1-4.5, the analytic solution for the density ρ, velocities V_x and V_y, temperature T and pressure p agree with the DSMC results within the discretization error. This confirms the study of Cai and Boyd [3] and the study of Khasawneh, Liu and Cai[8]. The agreement was expected, as both the analytical solution and DSMC result have the same inlet distribution 2.3 and solve the collisionless Boltzmann equation.

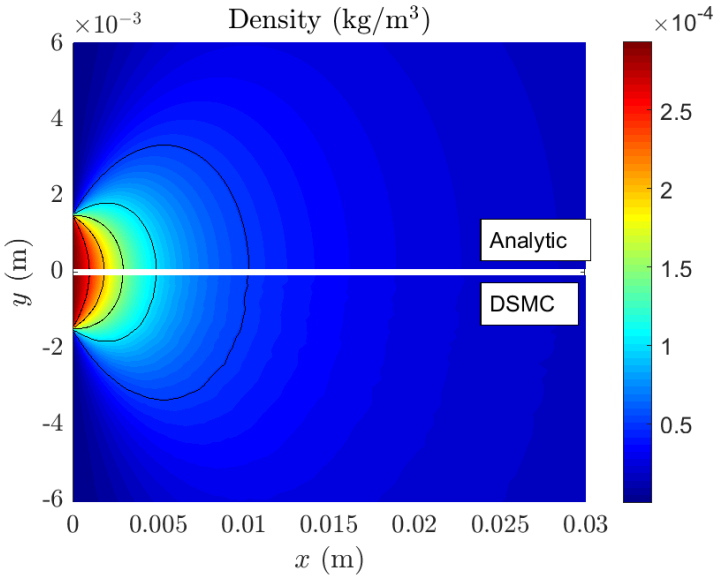

Figure 4.1: Comparison of density for the collisionless DSMC and analytical solution, for a single jet.

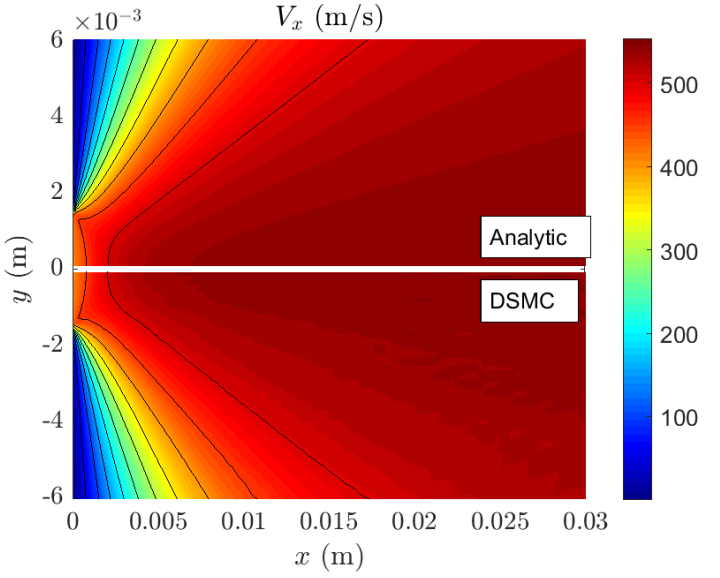

Figure 4.2: Comparison of average velocity in the x-direction for the collisionless DSMC and analytical solution, for a single jet.

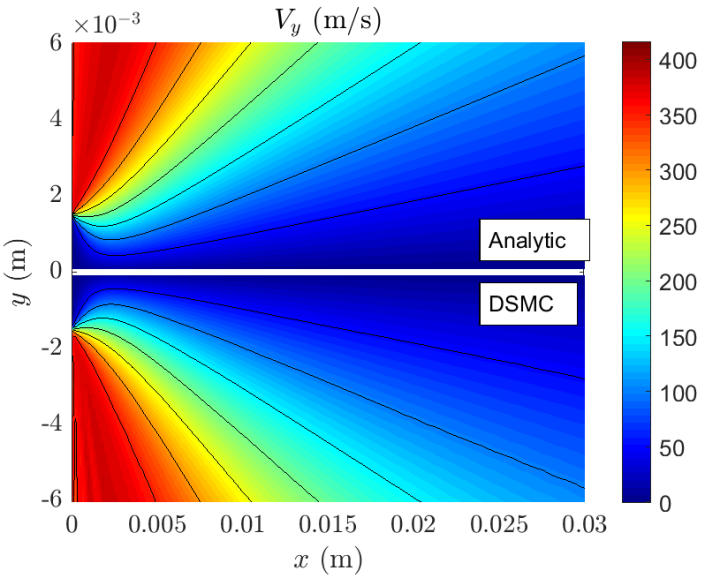

Figure 4.3: Comparison of average velocity in the y-direction for the collisionless DSMC and analytical solution, for a single jet.

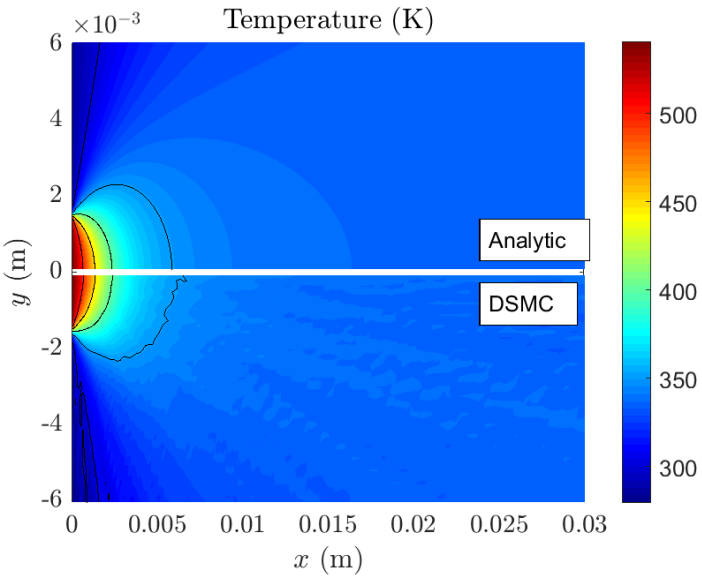

Figure 4.4: Comparison of temperature for the collisionless DSMC and analytical solution, for a single jet.

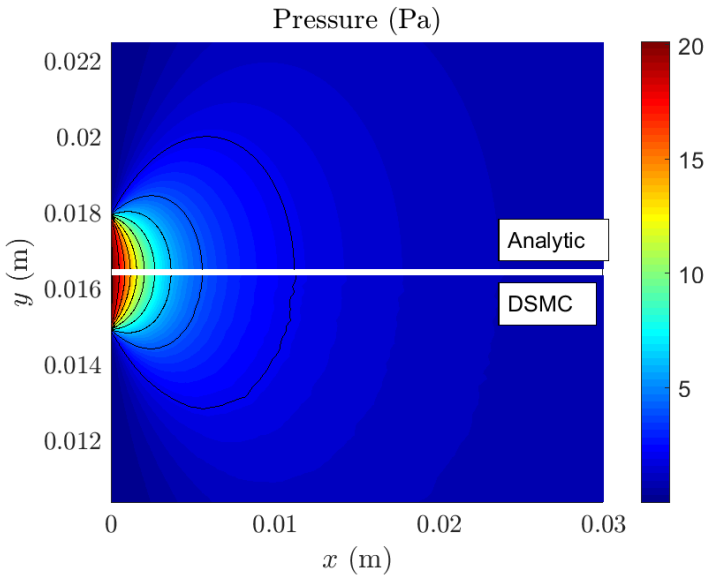

Figure 4.5: Comparison of pressure for the collisionless DSMC and analytical solution, for a single jet.

When particles collide their velocities change. This influences the behavior of the gas, which results in a deviation from the collisionless case. To observe the quantitative difference and the dependency of Kn_s, the analytical solution is compared to multiple DSMC results for single jet for different Kn_s values. Figure 4.6 compares the density of the collisionless analytical solution with the case $Kn = 0.05$. The density decreases more during the expansion for $Kn_s = 0.05$. The mass flow coming from the inlet is the same, which means that the gas should expand quicker. The magnitude of the velocities is compared in figure 4.7. As expected, the velocity is smaller for the collisionless case, which corresponds to the findings of the density. From the conservation of energy, it follows, that an increase in velocity comes along with a decrease of temperature (figure 4.8). The particles have a velocity in three dimensions. The thermal energy is distributed equally over the directions at the inlet. The thermal energy in z-direction is thus converted to kinetic energy through collisions. This conversion results in a different flow field, as for smaller Kn_s the mass flow becomes greater in the y-direction and thus lower in the x-direction. The simulation has also a back flow over the boundary at $x = 0$, but this can be neglected.

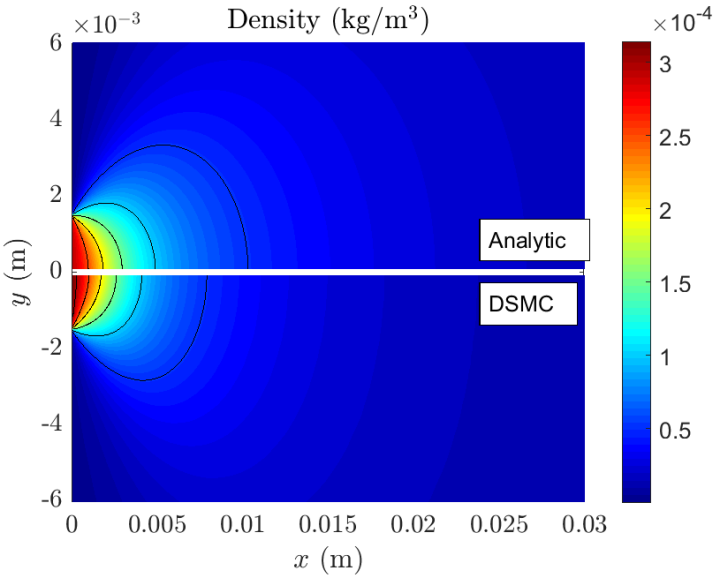

Figure 4.6: Comparison of density for the analytical solution and a DSMC for $Kn_s = 0.050$, for a single jet.

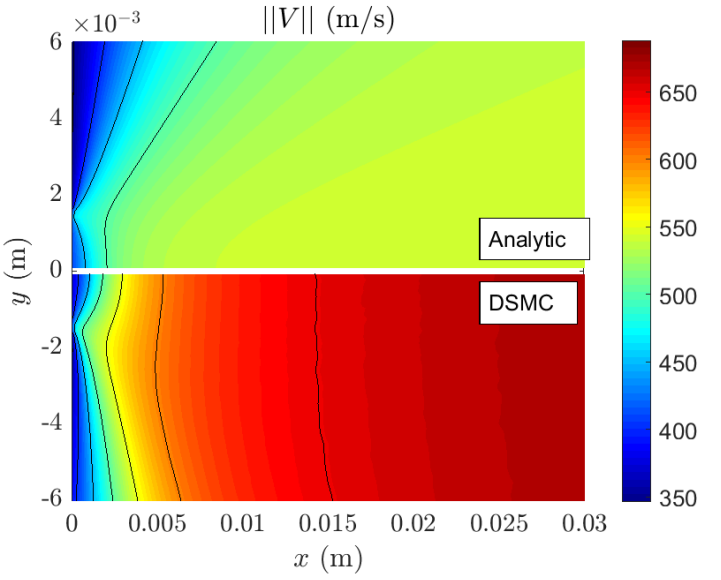

Figure 4.7: Comparison of average velocity for the analytical solution and a DSMC for $Kn_s = 0.050$, for a single jet.

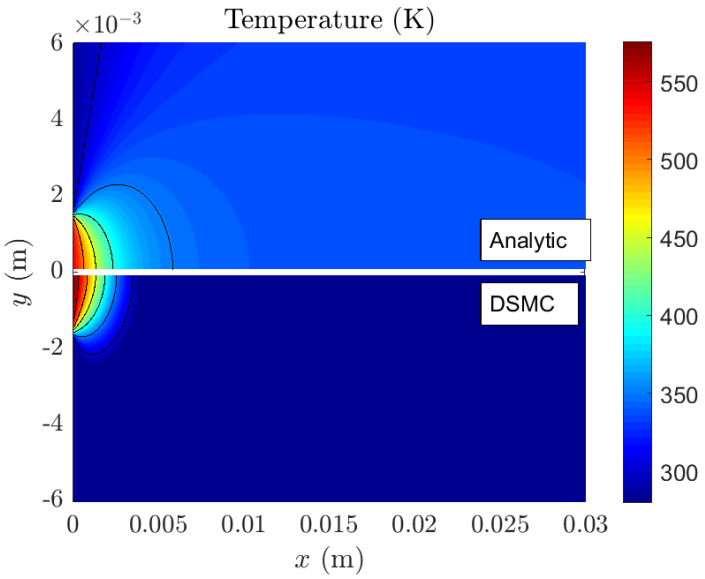

Figure 4.8: Comparison of the temperature for the analytical solution and a DSMC for $Kn_s = 0.050$, for a single jet.

We thus found that the collisionless case differs from the case with collision. To compare this difference, we looked at the horizontal line at $y = 0$. Figure 4.9 shows the ratio of the density between the DSMC result and analytical results for different Kn_s. It shows that the relative difference is higher for lower Kn_s and it depends on the position. For $Kn_s = 5$ the analytical solution is an accurate approximation, but this is not the case for lower stagnation Knudsen number. Furthermore, the density at the inlet is higher compared to the collisionless case. This results from the effect of back flow and is influence by collisions.
The density for a three-dimensional expansion in vacuum Li[9] approximates the density assuming $\rho \propto \frac{1}{R^2}$, with R the radial distance to the inlet. The $\frac{1}{R^2}$ term is independent of Kn_s. For our two-dimensional domain, this becomes $\propto \frac{1}{R}$. Which holds true for the collisionless case with $R > 3$mm. However, figure 4.9 contradicts that this is independent of Kn_s within the domain of interest, as the ratios decreases in the domain. The discrepancy can be explained by the conversion of thermal energy to kinetic energy. The thermal energy in the z-direction also acts like a reservoir, for which the collision frequency determines how fast this energy can be transformed to kinetic energy. This, as discussed before, influences the change in velocity and thereby the change in density. The method by Li[9], should thus not be used for stagnation Knudsen number above 0.05. The approximation was already flawed for small R, as the inlet is not a point source.

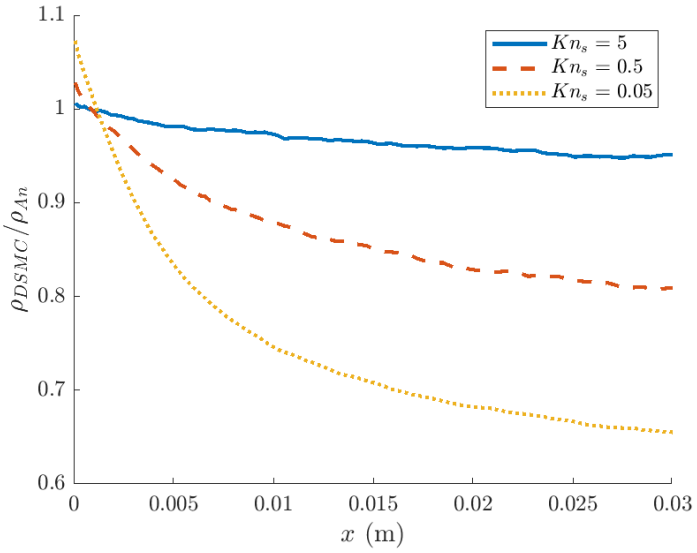

Figure 4.9: The density ratio between with and without collisions, for different Kn_s at $y = 0$.

4.2. DUAL JETS IN VACUUM

For the case of two jets in vacuum for the two dimensional case, the analytical solution is found by using the formulas for the single jet and combining them. With two inlets, there are two sets Ω_1 and Ω_2, corresponding to each inlets. The number density n_{dual} of the dual jet, can thus be expressed like equation 2.7a, by

$$n_{dual}(x,y) = \iiint_{\Omega_1 \cup \Omega_2} f_0 \, \mathrm{d}\boldsymbol{v}$$

In this equation the integral can be rewritten as two integrals, one for each set. This gives

$$n_{dual}(x,y) = \iiint_{\Omega_1} f_0 \, \mathrm{d}\boldsymbol{v} + \iiint_{\Omega_2} f_0 \, \mathrm{d}\boldsymbol{v}.$$

These integrals are the number density n_{solo} for a solo jet, i.e.

$$n_{dual}(x,y) = n_{solo,1} + n_{solo,2}. \tag{4.1}$$

The number density for dual jets is thus the summation of two solo jets.
The same approach can be used for the velocity $\boldsymbol{V}_{dual}$. Equation 2.7b can be used for dual inlets by again integrating over the two sets Ω_1 and Ω_2.

$$\boldsymbol{V}_{dual}(x,y) = \frac{1}{n_{dual}} \iiint_{\Omega_1 \cup \Omega_2} \boldsymbol{v} f_0 \, \mathrm{d}\boldsymbol{v}.$$

The integral in this equation is then divided by the sets, i.e.

$$\boldsymbol{V}_{dual}(x,y) = \frac{1}{n_{dual}} \left(\iiint_{\Omega_1} \boldsymbol{v} f_0 \, \mathrm{d}\boldsymbol{v} + \iiint_{\Omega_2} \boldsymbol{v} f_0 \, \mathrm{d}\boldsymbol{v} \right).$$

The integrals rewritten by using equation 2.7b. This gives the equation

$$\boldsymbol{V}_{dual}(x,y) = \frac{n_{solo,1}\boldsymbol{v}_{solo,1} + n_{solo,2}\boldsymbol{v}_{solo,2}}{n_{dual}}. \tag{4.2}$$

The velocity of the gas for dual jets, is thus the average velocity weighted by the number density.
The temperature T_{dual} of the dual jet is derived from the internal energy. Equation 2.7c, can be rewritten as two parts corresponding to the total energy e_T and kinetic energy e_{kin}. These are defined by

$$e_T = \frac{m}{k}\frac{1}{3n}\iiint ||\boldsymbol{v}||^2 f_0 \,\mathrm{d}\boldsymbol{v},$$
$$e_{kin} = \frac{m}{k}\frac{1}{3n}\iiint ||\boldsymbol{V}||^2 f_0 \,\mathrm{d}\boldsymbol{v}.$$

The second equation can be written as $e_{kin} = \frac{m}{k}\frac{||\boldsymbol{V}||^2}{3n}$, because $\boldsymbol{V}$ in a constant in the integral. Rewriting the equation for T_{dual}, gives us

$$T_{dual} = -\frac{m}{k}\frac{||\boldsymbol{V}_{dual}||^2}{3} + \frac{m}{3k}\frac{n_{solo,1}e_{T,solo,1} + n_{solo,2}e_{T,solo,2}}{n_{dual}}. \tag{4.3}$$

In this equation $e_{T,solo}$ stands for the part corresponding to one inlet. Which is expressed in appendix A.
These equations for collisionless dual jets expansion in vacuum are then compared with a collisionless DSMC simulation. These results are found in figures 4.10-4.15. These figures confirm that the analytical solution is equal to the DSMC results within the bounds of the statistical error. The equations discussed are not only useful for the collisonless case. If the result of a single jet simulation is used, then the equations still holds. This gives the collisionless effect between jets, which can be used to compare the difference in effect for all the macroscopic properties.

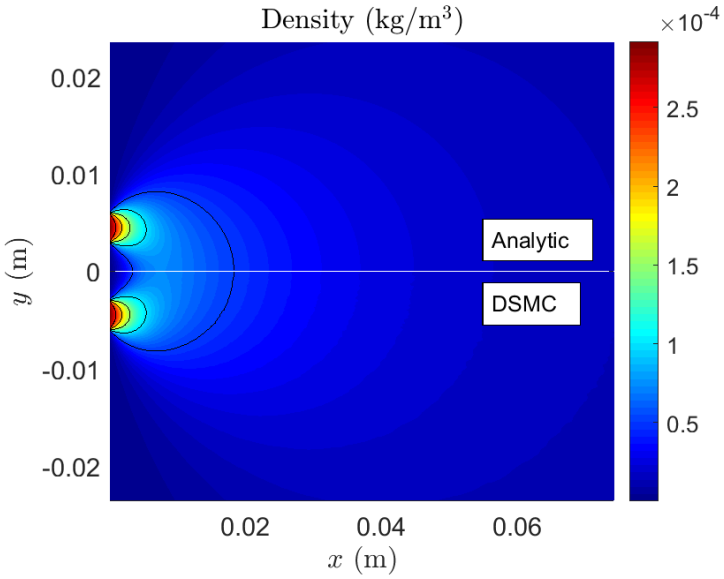

Figure 4.10: Comparison of density for the collisionless DSMC and analytical solution, for two jets.

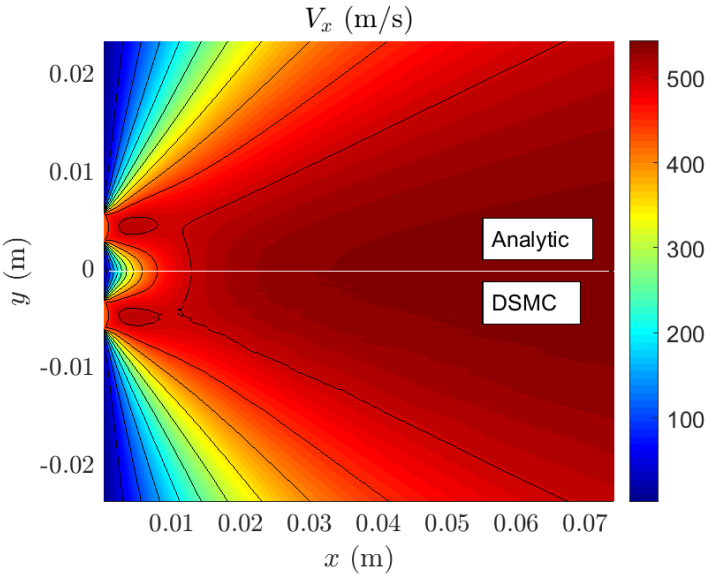

Figure 4.11: Comparison of average velocity in the x-direction for the collisionless DSMC and analytical solution, for two jets.

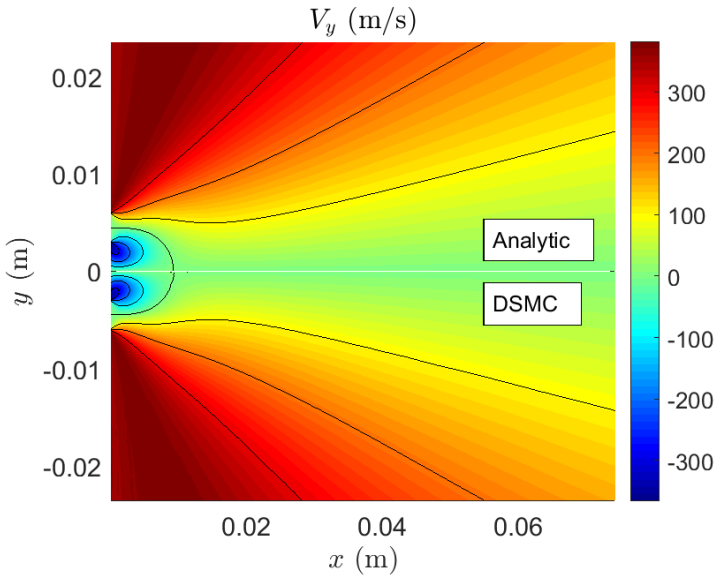

Figure 4.12: Comparison of average velocity in the y-direction for the collisionless DSMC and analytical solution, for two jets.

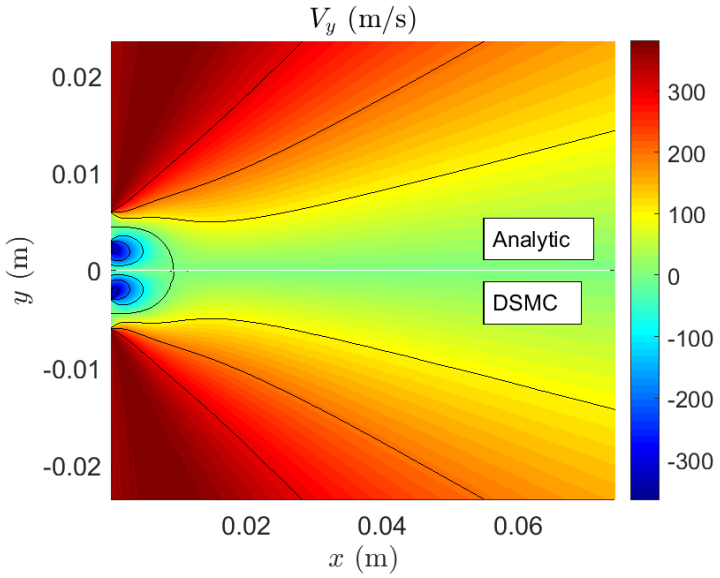

Figure 4.13: Comparison the velocity magnitude for the collisionless DSMC and analytical solution, for two jets.

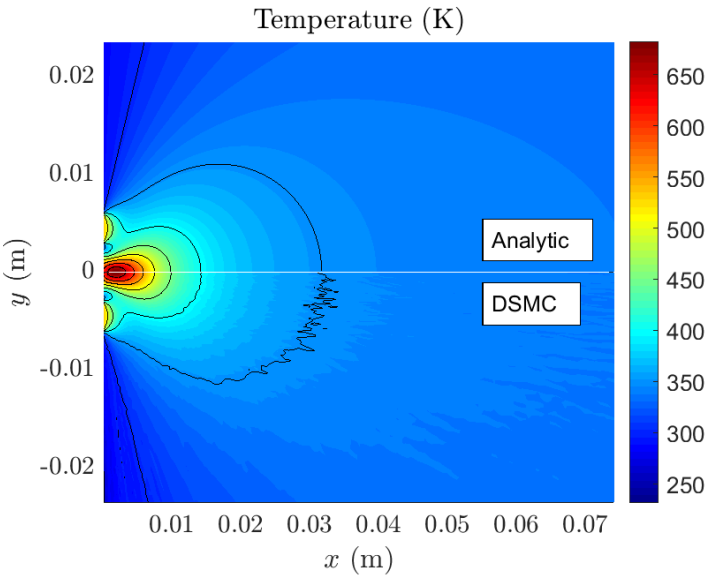

Figure 4.14: Comparison of temperature for the collisionless DSMC and analytical solution, for two jets.

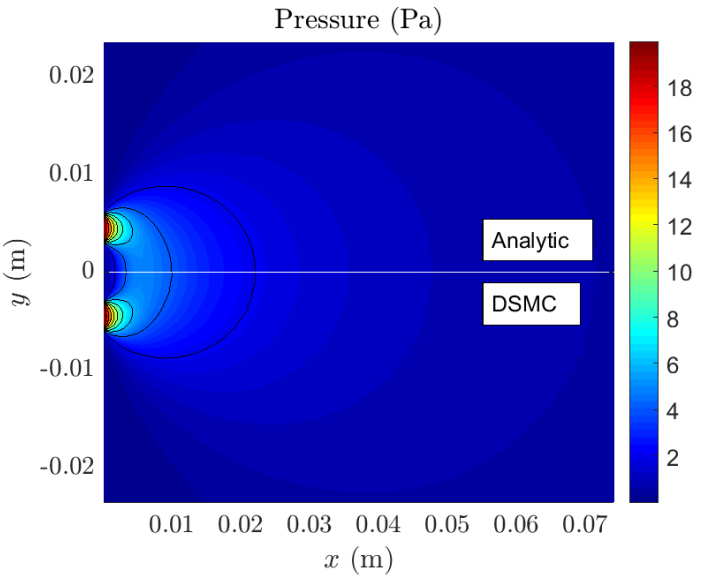

Figure 4.15: Comparison of pressure for the collisionless DSMC and analytical solution, for two jets.

5

INTERACTION BETWEEN THE JETS

A shock wave can occur when two vapor jets interact with each other. This happens when the penetration Knudsen number Kn_p is small enough. Particles from both jets will then collide. These particles have a high relative velocity in y-direction and thus a high thermal energy. Through collisions, this thermal energy is converted to the other directions. These particles do thus not penetrate the other jet, but will stay between the jets. This gas has thus a high density and low flow velocity, which acts as a wall for the approaching particles. This results in a shock wave. Figures 5.1-5.7 show the properties for $Kn_s = 0.0065$ and $l = 4.5$mm, with the inlet from 3mm to 6mm. The domain is extended by the use of symmetry. This case has a shock which results into a secondary jet. The shock occurs were there is an abrupt increase in density, shown in figure 5.1. The area unaffected by the shock wave has the same properties compared to the solo jet. This area is thus unaffected by the interaction and can be used in calculating $Kn_{p,min}$. The shock changes the gas flow direction, shown in figure 5.3. The secondary jet is similar to the three-dimensional case [7]. Both have a lower density in the middle of secondary jet.

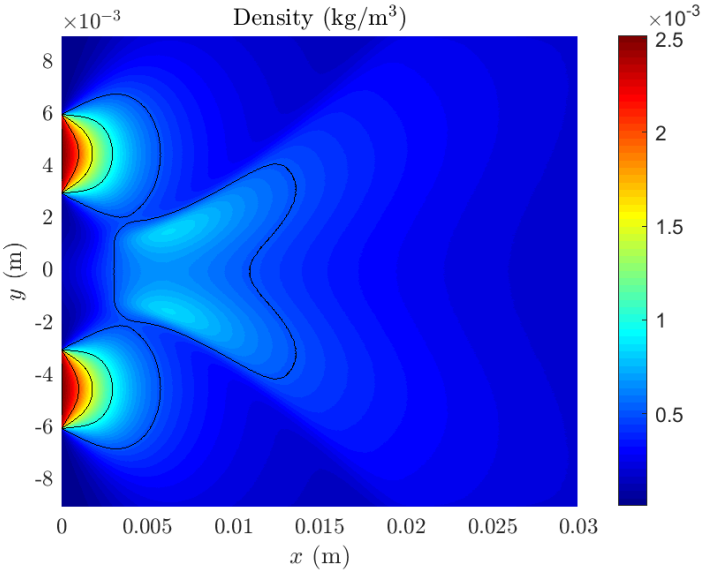

Figure 5.1: Contours of the density for two interacting jets with inlet condition $Kn_s = 0.0065$ and separation distance $l = 4.5$mm.

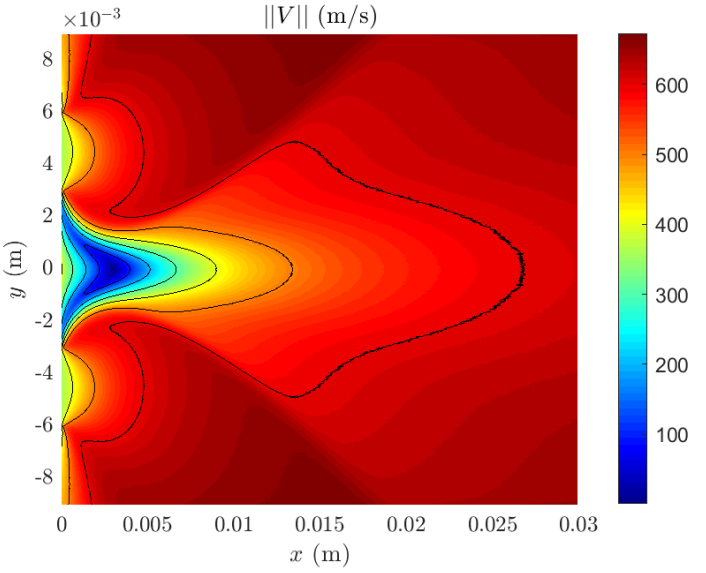

Figure 5.2: Contours of the magnitude of the velocity for two interacting jets with inlet condition $Kn_s = 0.0065$ and separation distance $l = 4.5$mm.

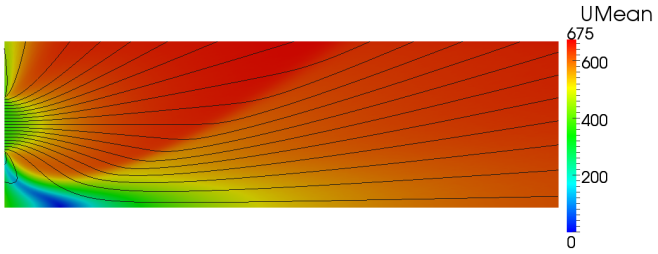

Figure 5.3: Contours of the magnitude of the velocity with gas flow direction, for two interacting jets with inlet condition $Kn_s = 0.0065$ and separation distance $l = 4.5$mm.

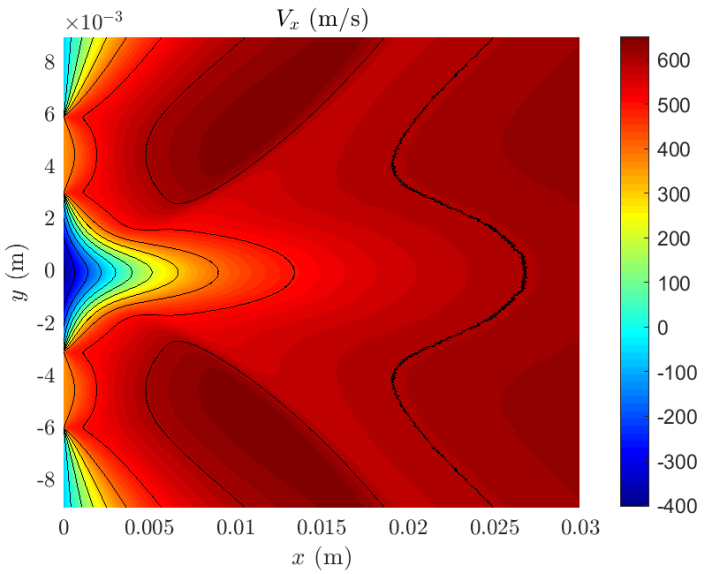

Figure 5.4: Contours of the velocity V_x for two interacting jets with inlet condition $Kn_s = 0.0065$ and separation distance $l = 4.5$mm.

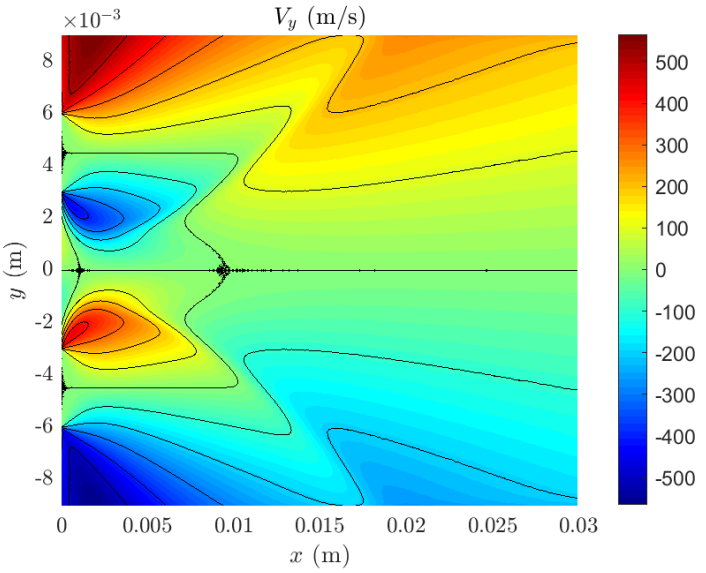

Figure 5.5: Contours of the velocity V_x for two interacting jets with inlet condition $Kn_s = 0.0065$ and separation distance $l = 4.5$mm.

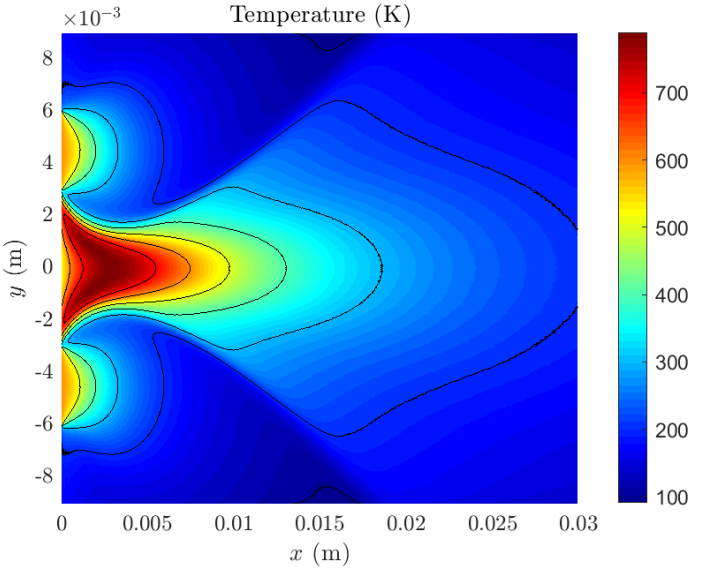

Figure 5.6: Contours of the temperature for two interacting jets with inlet condition $Kn_s = 0.0065$ and separation distance $l = 4.5$mm.

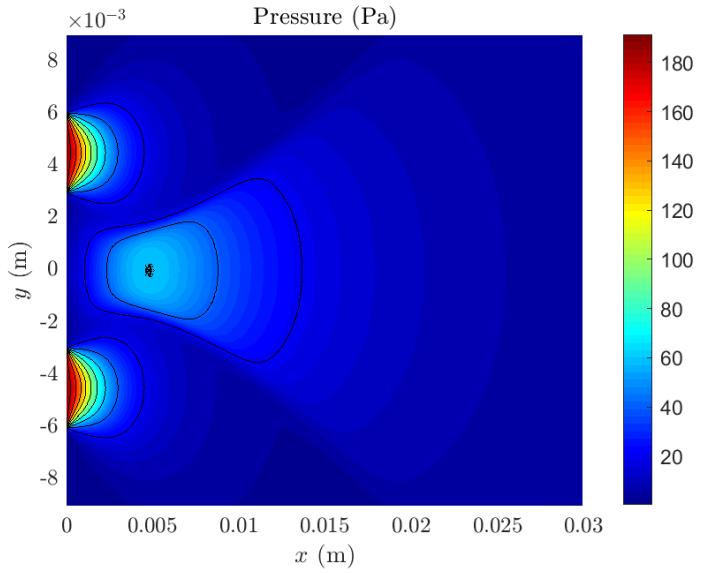

Figure 5.7: Contours of the pressure for two interacting jets with inlet condition $Kn_s = 0.0065$ and separation distance $l = 4.5$mm.

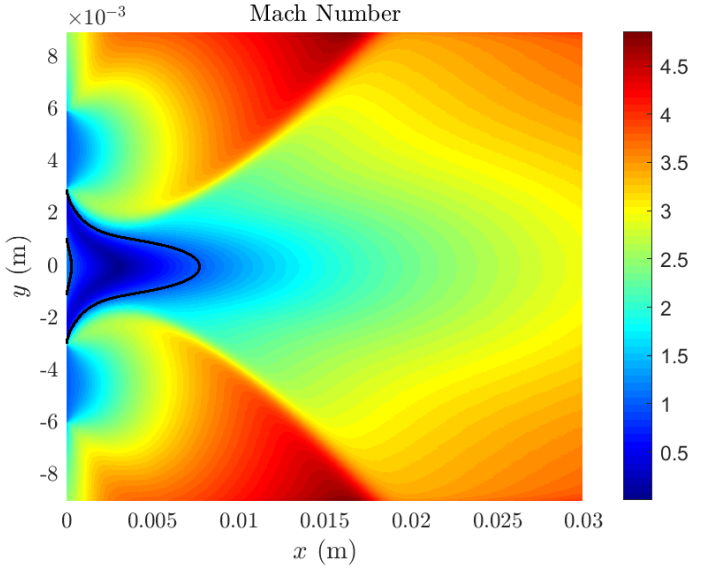

Figure 5.8: Contours of Mach number for two interacting jets with inlet condition $Kn_s = 0.0065$ and separation distance $l = 4.5$mm, with the black line at $M = 1$, dividing subsonic and supersonic.

5.1. THE INTERACTION EFFECT OF STAGNATION KNUDSEN NUMBER

When the particles of both jets collide with each other, the gas flow changes as the jets interact. This depends on the frequency of collisions, which is influenced by the density and thus by Kn_s. The collisionless case has no interaction, but for $Kn_s = 0.0065$ (figure 5.1) the interaction results in a shock wave. The interaction effect can be classified by the minimum penetration Knudsen number $Kn_{p,min}$. Figure 5.9 shows $Kn_{p,min}$ depending on Kn_s for different simulations with $l = 4.5$mm. Here $Kn_{p,min}$ depends linear on Kn_s with $Kn_{p,min} \approx 7.6 Kn_s$.

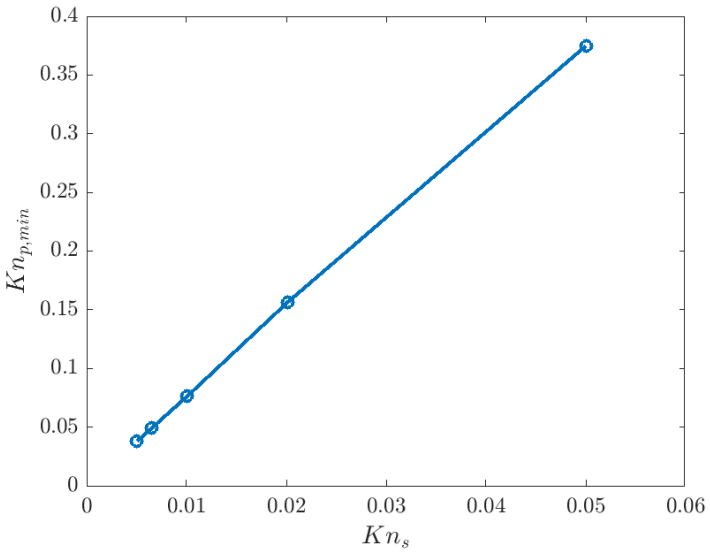

Figure 5.9: The minimum penetration Knudsen number depending depending on the stagnation Knudsen number, for different simulation with separation distance $l = 4.5$mm.

Figure 5.10 shows the density field for $Kn_s = 0.05$. Compared to the analytical solution (figure 4.10), there is a small but noticeable difference, which is that the density contour lines are less round compared to the collisionless case. For $Kn_s = 0.02$, shown in figure 5.11, there is a clear difference compared to the collisionless case and the contour lines looks like the those of $Kn_s = 0.0065$. However, there is no clear shock. Taking $Kn_s = 0.01$ (figure 5.12) gives a small and broad shock compared to $Kn_s = 0.0065$ with the same contour lines. The results for $Kn_s = 0.005$, shown in 5.13, looks the same as $Kn_s = 0.0065$ but has a sharper shock (figure 5.15).

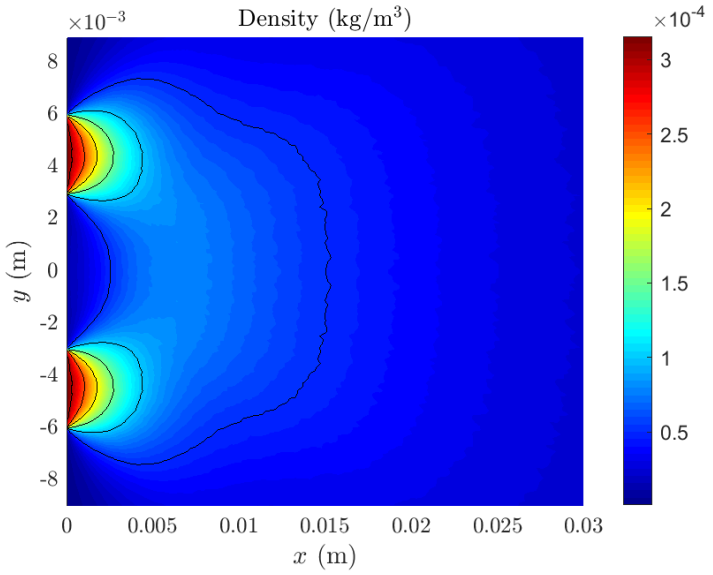

Figure 5.10: Contours of the density for two interacting jets with inlet condition $Kn_s = 0.05$ and separation distance $l = 4.5$mm.

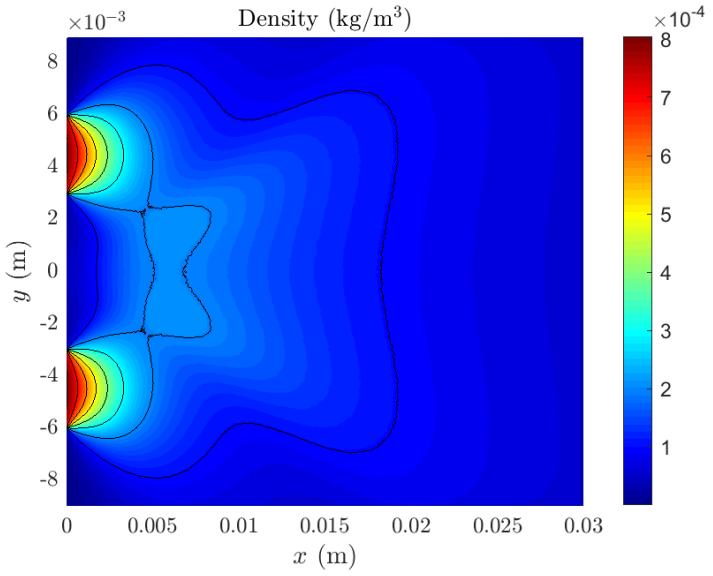

Figure 5.11: Contours of the density for two interacting jets with inlet condition $Kn_s = 0.02$ and separation distance $l = 4.5$mm.

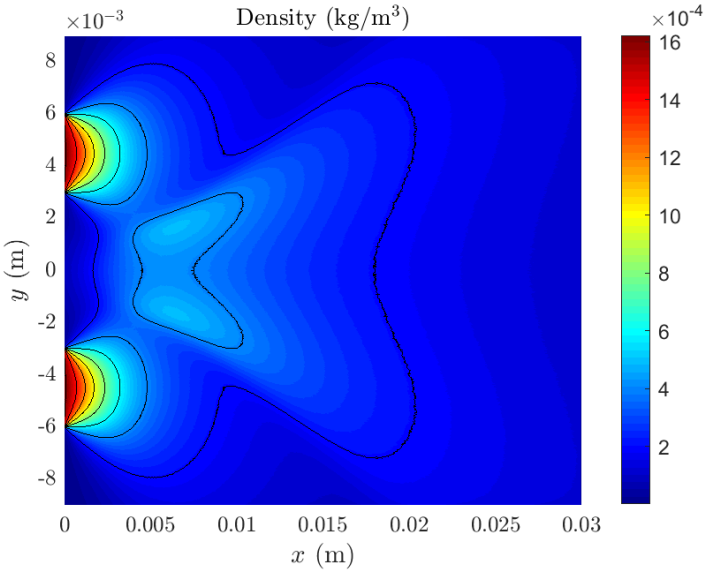

Figure 5.12: Contours of the density for two interacting jets with inlet condition $Kn_s = 0.01$ and separation distance $l = 4.5$mm.

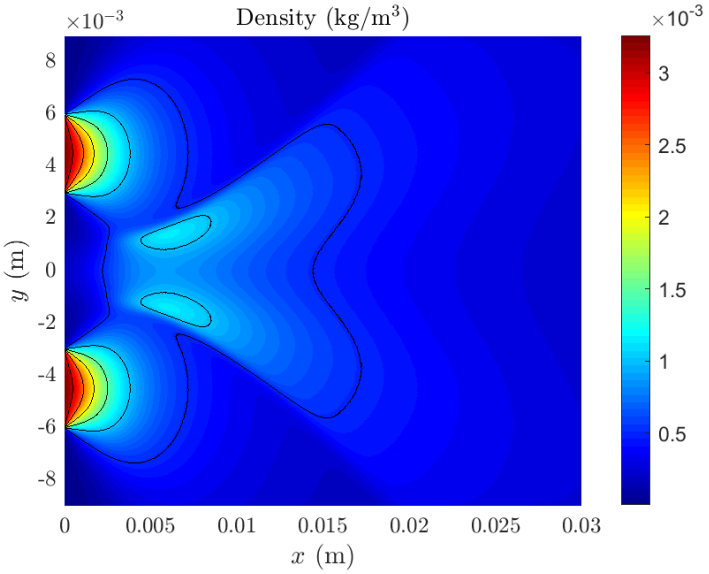

Figure 5.13: Contours of the density for two interacting jets with inlet condition $Kn_s = 0.05$ and separation distance $l = 4.5$mm.

The interaction effect can also be observed by the mass flow over the the jet axis, i.e.

line $y = l = 4.5$mm. The mass flow from a single jet is zero over this line, and thus all mass flow results from the other jet and its interaction. The mass flow over the line from 0 to x are shown in figure 5.14. The mass flows are normalized by the mass flow through the inlet $\dot{m}_{in}$. The interaction between the jets changes the mass flow across the jet axis. The mass total mass flow is unchanged. The interaction effect moves the mass flow further over the line. When a shock occurs, the mass flow becomes close to zero before a certain point and is thus halted. Figure 5.15 shows the density on the line $y = l = 4.5$ for the different Kn_s. The figures shows a shock for the lower Kn_s, which becomes narrower for smaller Kn_s.

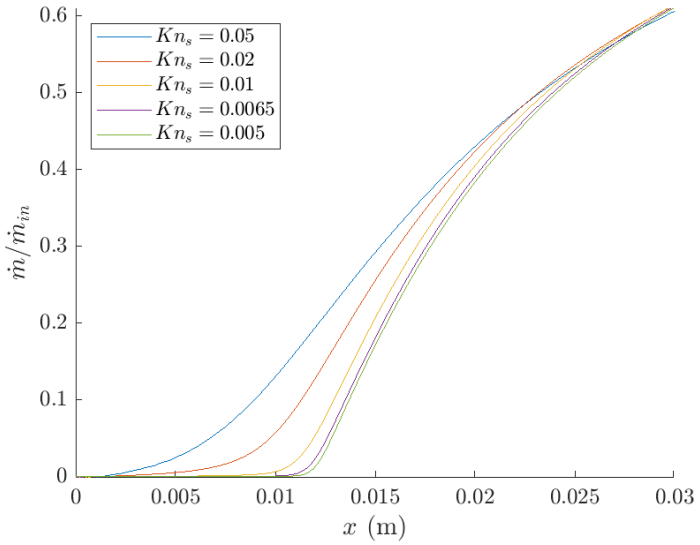

Figure 5.14: The normalized mass flow over the line $y = 4.5$mm till the point x, for different Kn_s.

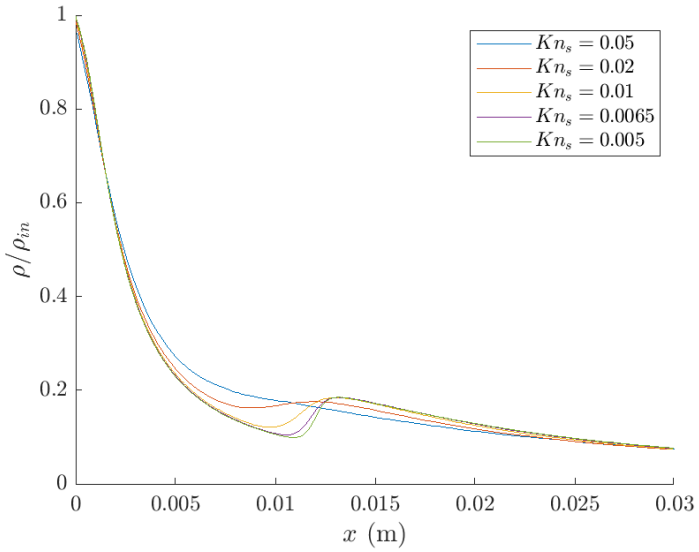

Figure 5.15: The relative density at the axis of the inlet, i.e. $y = l$, for different Kn_s.

5.2. THE EFFECT OF THE DISTANCE BETWEEN THE JETS

The distance between the center of the inlet and the symmetry line is denoted l. This distance influences the interaction effect. Following equation 2.13, Kn_p is calculated by using the number density from a single jet (figure 5.16). Here l starts from 1.5mm= $h/2$, at which the two inlets are merged to one. This figures shows that a stronger interaction should be observed for smaller l as Kn_p becomes smaller. However, this is not found in the results of the DSMC. Take for example $l = h/2$, the two inlets are connected and can be simulated by one, which has no shock. For $l \ll h/2$, the two jets behave like a single larger one. Figure 5.17 shows the density for the case with $l = 0.05$mm, here the density field is similar to a single jet case. Taking $l = 0.5$ results in a shock, however the shock extends less far compared to figure 5.1. These results contradict with Kn_p (figure 5.16). This is caused by the definition of Kn_p, which does not take the size of the inlet into account.

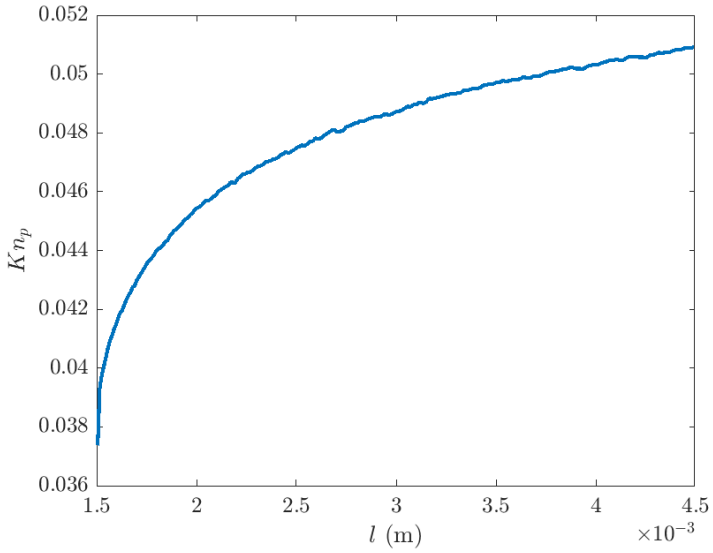

Figure 5.16: The minimum penetration Knudsen number depending on the distance between jets.

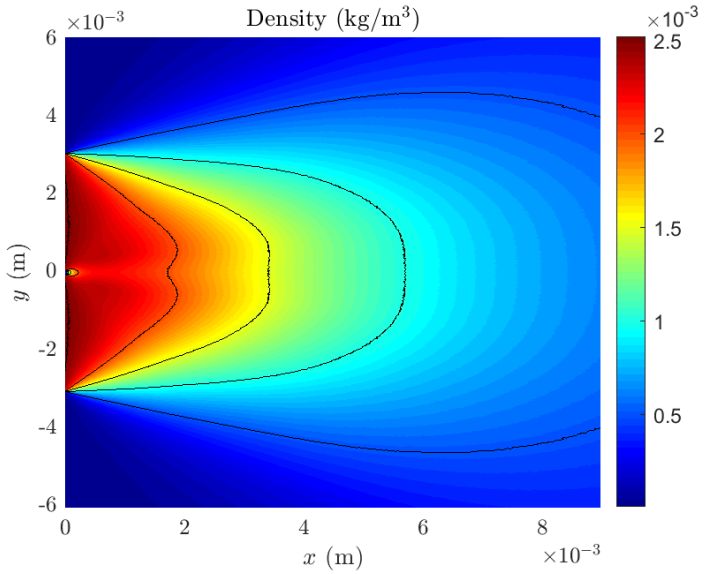

Figure 5.17: Contours of the density for two interacting jets with inlet condition $Kn_s = 0.0065$ and separation distance $l = 2.0$mm.

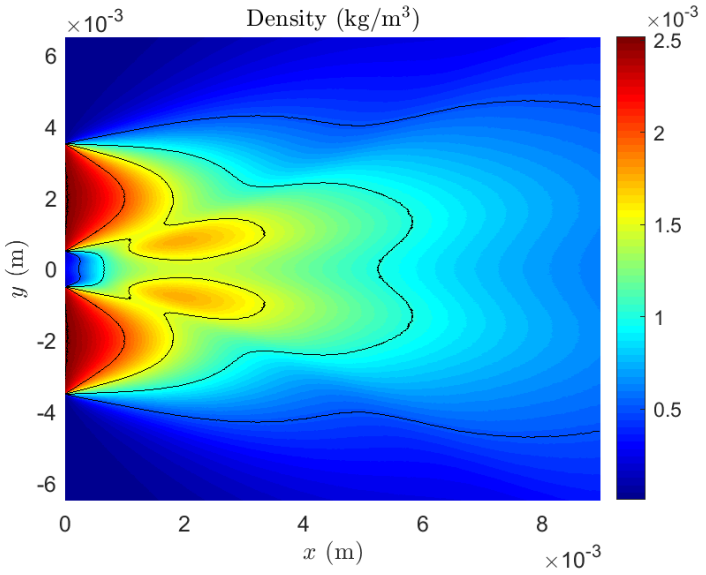

Figure 5.18: Contours of the density for two interacting jets with inlet condition $Kn_s = 0.0065$ and separation distance $l = 1.55$mm.

Figure 5.19 and 5.20 shows the density profile for $l = 3.0$mm and $l = 7.5$mm. The other properties can be found in appendix B. These profiles are similar to a scaled version of $l = 4.5$mm (figure 5.17), with a reduces density at the shock profile for larger l as the gas expends. Figure 5.21 shows the density over the line $y = l$ relative to the inlet density. For small x the mass flow is the same. This is expected, as before the shock the density is equal to that of a single jet. The density increases sharply at the point the shock passes the line $y = l$, after which the density decreases like an expansion. However, the density is higher for larger values of l, after the shock. The effect on the density of the second jet thus becomes stronger the farther the two jets are. This is different compared to the collisionless case, for which further distance between jets results in a smaller effect on the density.

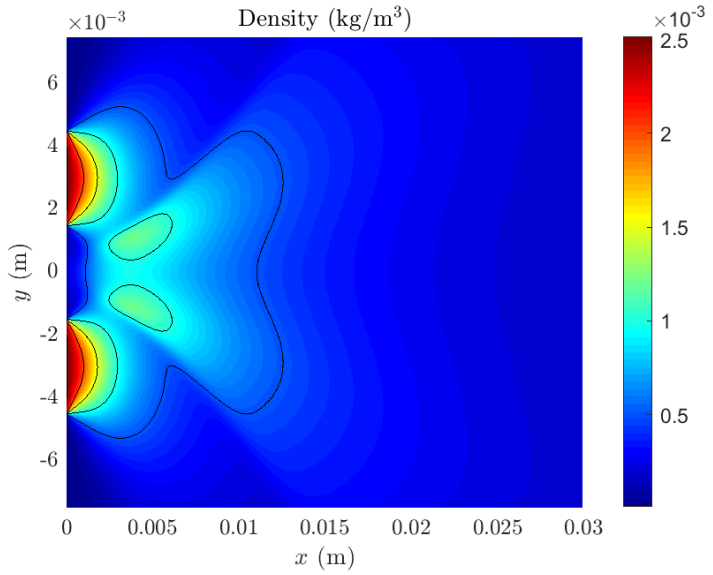

Figure 5.19: Contours of the density for two interacting jets with inlet condition $Kn_s = 0.0065$ and separation distance $l = 3.0$mm.

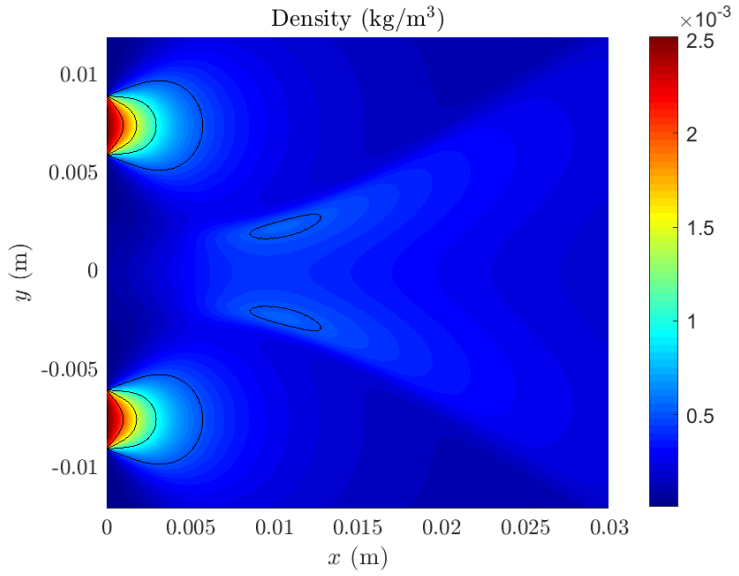

Figure 5.20: Contours of the density for two interacting jets with inlet condition $Kn_s = 0.0065$ and separation distance $l = 7.5$mm.

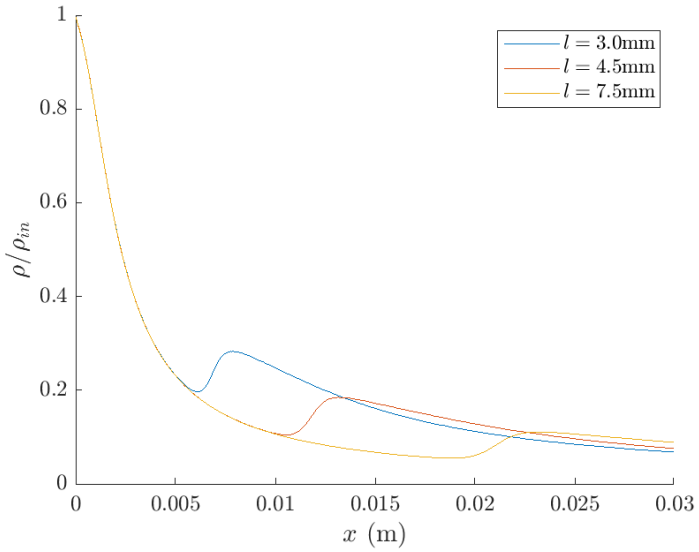

Figure 5.21: The density at the axis of the inlet, i.e. at $y = l$, for different l with $Kn_s = 0.0065$.

Figure 5.22 shows the mass flow rate $\dot{m}_{pen}$ over the line $y = l$ from 0 to x. These lines are similar to each other. Scaling x by the inverse of $l - b$ with $b = 0.5$mm gives two comparable functions, shown in figure 5.23. The two functions can be approximated by each other with equation

$$\dot{m}_{pen}(x, l_1) \approx \dot{m}_{pen}\left(x\frac{l_2 - b}{l_1 - b}, l_2\right). \tag{5.1}$$

The value of b can be changed to get a better approximation for a certain x. If b is taken as function of x, then the approximation becomes an equality. This approximation is also true for different Kn_s. The comparison for $Kn_s = 0.05$ is shown in figure 5.24.

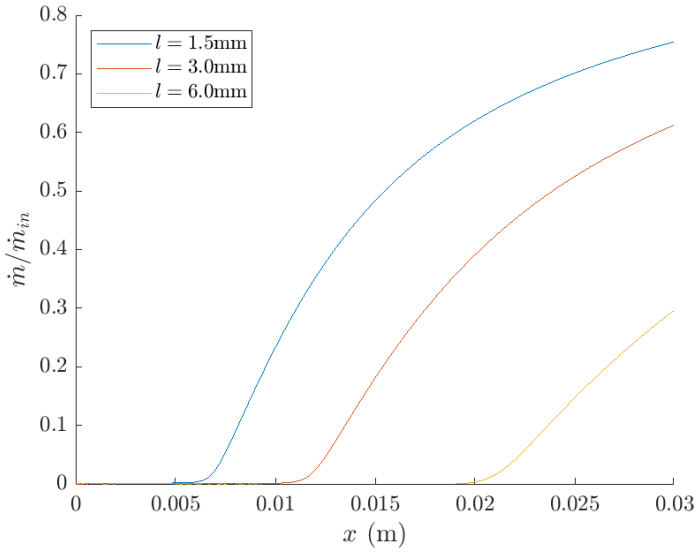

Figure 5.22: The mass flow rate over the line $y = l$ from 0 to x, for different simulations with $Kn_s = 0.0065$.

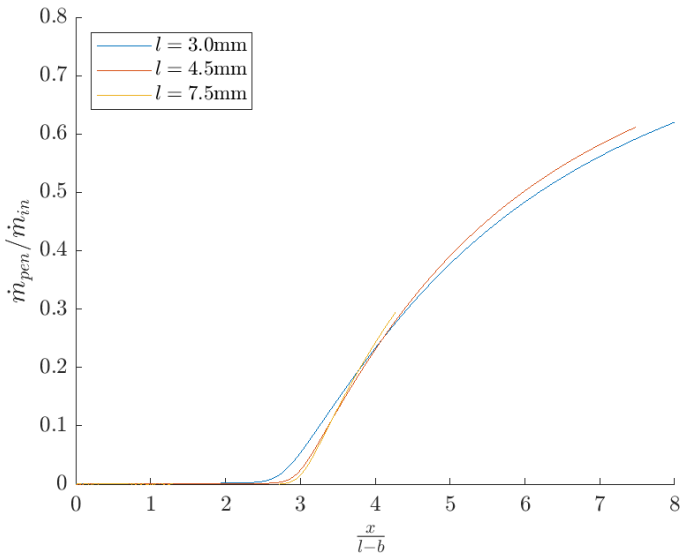

Figure 5.23: The mass flow rate depending on $\frac{x}{l-b}$ with $b = 0.5$mm, over the line $y = l$ from 0 to x, for different simulations with $Kn_s = 0.0065$.

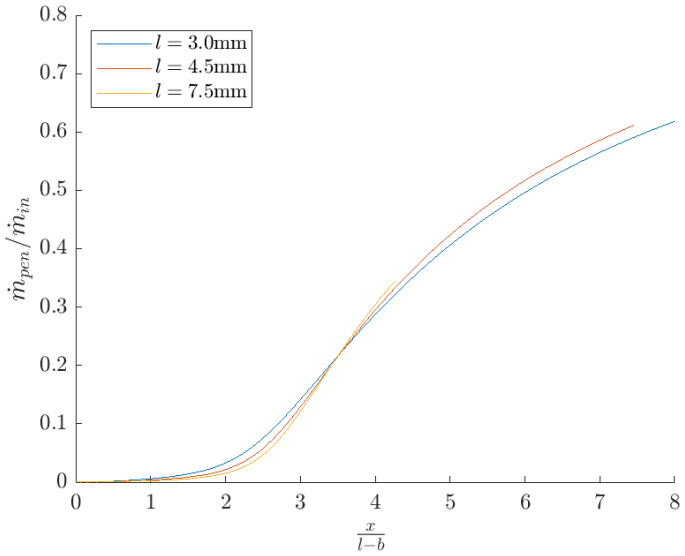

Figure 5.24: The mass flow rate depending on $\frac{x}{l-b}$ with $b = 0.5$mm, over the line $y = l$ from 0 to x, for different simulations with $Kn_s = 0.05$.

6

Optimizing Vapor Deposition

Coating a metal sheet with zinc can be done by Physical Vapor Deposition. The zinc vapor from the source will expand into vacuum and attach to the metal, forming a coating. Using our setup of two jets, we find the optimal coating depending on the parameters stagnation Knudsen number Kn_s, distance between jets l and distance between the inlet and the sheet d. Figure 6.1 shows the setup.

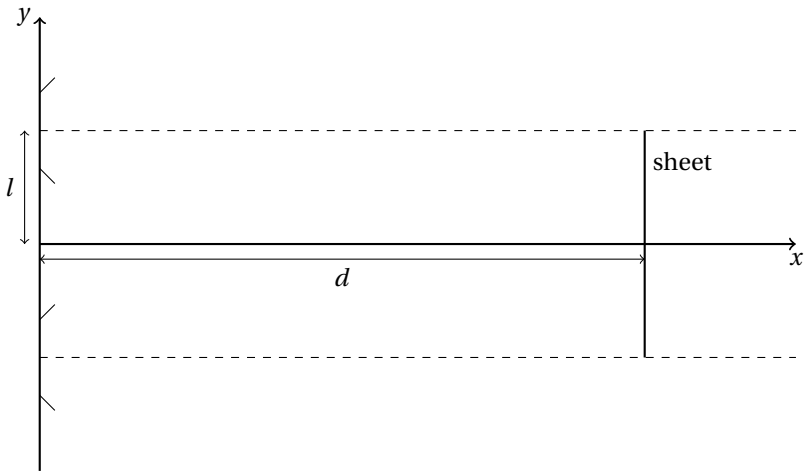

Figure 6.1: Visualization of the optimization problem.

The optimal coating is found by using an optimization problem. We want to optimize a cost function c, with constraints $\boldsymbol{g}$. This gives the optimization problem:
Find d, l, Kn_s to

$$\begin{array}{ll} \text{maximize} & c(d,l,Kn_s) \\ \text{subject to} & \boldsymbol{g}(d,l,Kn_s) > 0, \\ & 10\text{mm} \le d \le 30\text{mm}, \\ & 3.0\text{mm} \le l \le 7.5\text{mm}, \\ & 0.005 \le Kn_s \le 0.05, \end{array}$$

The domain for Kn_s is chosen to include the jet interaction effect ranging from small interaction to a clear shock. The length between inlets l has a lower bound for practical constraints. The constraints for d are caused by practical limitations, as for a smaller value the gas has no room to expand and high values of d are inefficient.
In this section, we will define the optimal coating as the highest deposition speed, while being applied uniformly. An approximation for the cost function and constraint is found and how this results in a faster search method.

6.1. COST FUNCTION

For practical use, we are interested in vapor deposition with multiple jets. Therefore, we look at the mass flow rate of the area between the jets, as for multiple jets the plate can be partitioned. We optimize the coating by the coating speed. A faster coating speed results in a higher production. The coating speed depends on the mass flow rate over the area of the sheet. The mass flow rate over an area A is expressed by

$$\dot{m} = \iint_A \rho \boldsymbol{V} \cdot \mathrm{d}A. \tag{6.1}$$

The mass flow rate $\dot{m}_{coat}$ over the sheet can be expressed by

$$\dot{m}_{coat} = \int_0^l \rho V_x \,\mathrm{d}y. \tag{6.2}$$

Figure 6.2 shows an example of ρV_x. The mass flow rate has the unit kg $\mathrm{s}^{-1}\mathrm{m}^{-1}$ as the size of the z-direction is arbitrary. Using the symmetry boundary at $y = 0$, the setup is shown in figure 6.3.

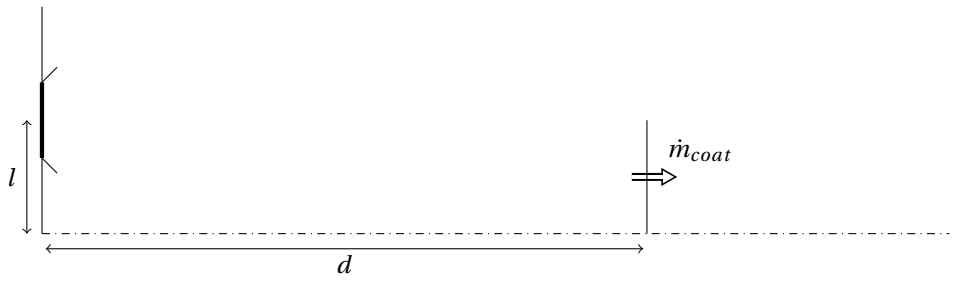

Figure 6.3: The mass flow rate $\dot{m}_{coat}$ over the sheet, distance d behind the inlet.

The coating speed is proportional to $\frac{\dot{m}_{coat}}{l}$. Optimizing the coating speed can thus be done by maximizing

$$c(d,l,Kn_s) = \frac{\int_0^l \rho V_x \,\mathrm{d}y}{l}, \tag{6.3}$$

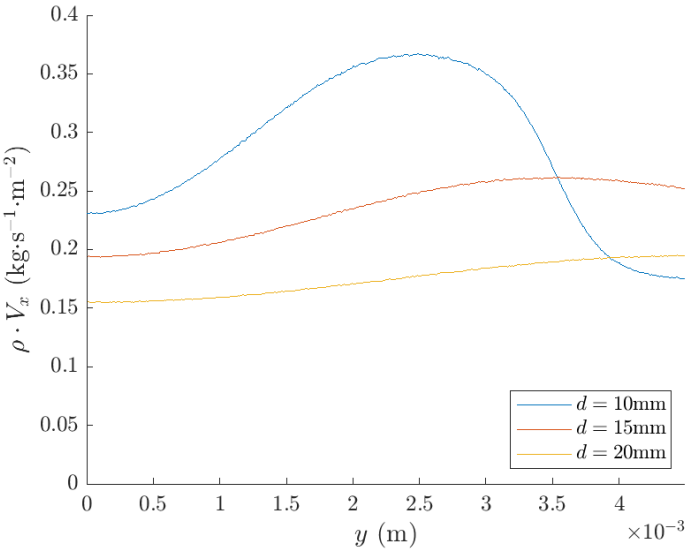

Figure 6.2: The vapor deposition ρV_x, for $Kn_s = 0.0065$ and $l = 4.5$mm, for different positions d of the sheet.

which has the unit kg s^{-1}m^{-2}. The sheet is assumed to not alter the gas flow. Therefore, a simulation contains the entire domain of d. A new simulation is thus only needed for different l and Kn_s. The simulations are in a steady state, the mass contained in an arbitrary volume remains the same. That means that the total flux over the boundary is zero, which can be expressed by $\oint_S \rho \boldsymbol{v} \cdot \hat{\boldsymbol{n}}\, ds = 0$. We are interested in the area between the jets shown in figure 6.4.

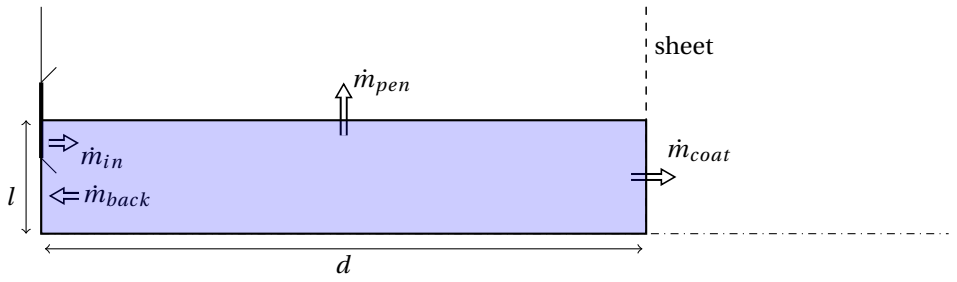

Figure 6.4: Visualization of the mass flow. The sheet is not simulated.

The boundary of this area can be divided in five parts, the symmetry line, the boundary at the sheet, the boundary over the axis of the jet, the inlet and the boundary below the inlet. The mass flow at the inlet $\dot{m}_{inlet}$ and the mass flow between the inlet and symmetry line or back flow $\dot{m}_{back}$ are both independent of d. The mass flow rate across the

symmetry boundary is zero. The cost function depends on the mass flow rate across the sheet. The mass flow rate of the coating can be written as

$$\dot{m}_{coat}(d) = \dot{m}_{inlet} - \dot{m}_{back} - \dot{m}_{pen}(d), \tag{6.4}$$

where $\dot{m}_{pen}$ stands for the mass flow crossing the middle of the jet, which depends on d, as shown in figure 6.4. The cost function can therefore be rewritten as

$$c = \frac{\dot{m}_{in} - \dot{m}_{back} - \dot{m}_{pen}}{l}. \tag{6.5}$$

The mass flow rate at the inlet $\dot{m}_{in}$ can be approximated by $\rho_0 V_{x,0} h$, which are the inlet density and inlet velocity. However, not all particles are simulated. The particles with negative v_x are not generated. The mass flow ignoring collision is calculated by

$$\dot{m}_{inlet} = h\rho_0 \int_{-V_{x,0}}^{\infty} f_x \mathrm{d}v_x \int_{-V_{x,0}}^{\infty} v_x f_x \mathrm{d}v_x$$

with f_x the Maxwell-Boltzmann distribution from equation 2.5. Solving the integrals gives

$$\dot{m}_{inlet,An} = h\rho_0 \left[\frac{V_{x,0}}{1 + \mathrm{erf}(V_{x,0}\beta)} + \frac{1}{2\sqrt{\pi\beta}} \exp\left(-\beta V_{x,0}^2\right) \right], \tag{6.6}$$

with $\beta = \sqrt{m/2kT_0}$. This is the mass flow rate generated by the DSMC. However, there is a difference between this and the observed mass flow. This is caused by particles moving back through the inlet, which are then deleted. The particles going back accounts for $0.03\dot{m}_{inlet,An}$. This is shown in figure 6.5. The relative number of particles lost through the inlet does increase for lower Kn_s, but this difference is neglected.

The back flow $\dot{m}_{back}$ depends on both the distance between inlets l and stagnation Knudsen number Kn_s. Figure 6.6 shows the back flow relative to $\dot{m}_{inlet}$. It shows that $\dot{m}_{back}$ depends on l and is consistent for Kn_s under a certain value. The values with $Kn_s = 0.05$ have a higher inaccuracy caused by larger cells.

The penetration mass flow rate $\dot{m}_{pen}$ for different l, shown in figures 5.23 and 5.24, are similar. It was found that $\dot{m}_{pen}(d, l_1) \approx \dot{m}_{pen}\left(d\frac{l_2-b}{l_1-b}, l_2\right)$, for a certain b around 0.5mm depending on d. The cost function can thus be approximated under certain conditions.

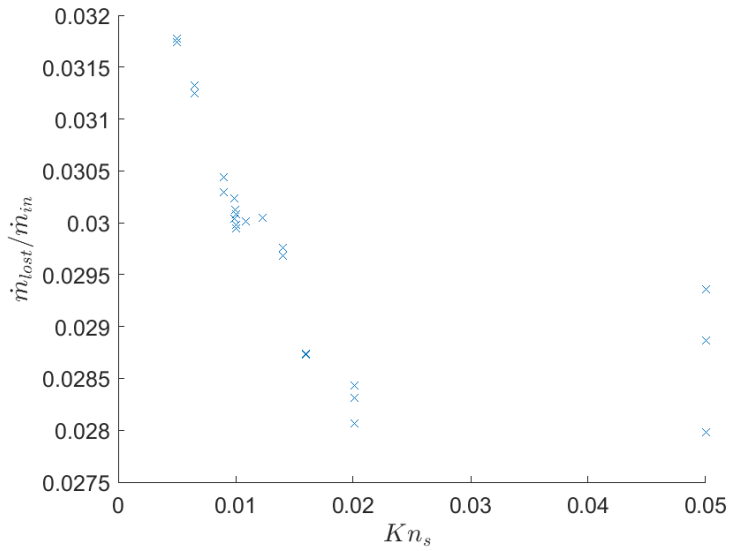

Figure 6.5: The relative mass flow rate lost through the inlet, for different inlet condition Kn_s and distance between jets l.

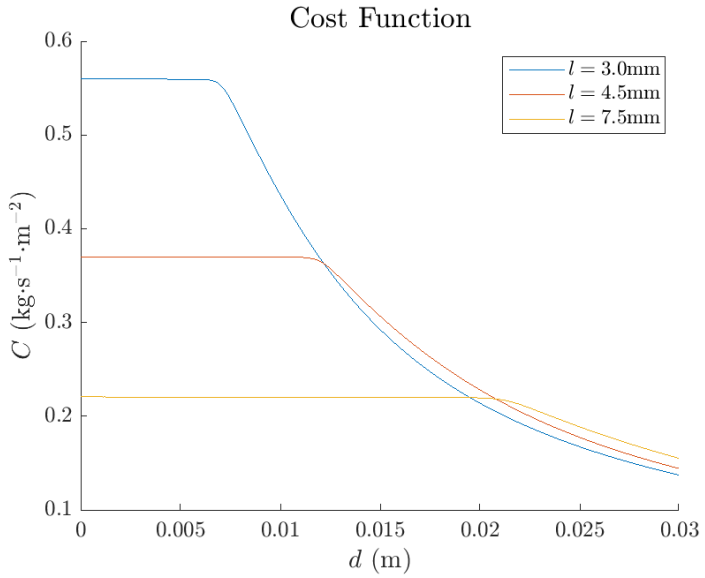

Figure 6.7: The cost function c depending on the position of the sheet d, for $Kn_s = 0.005$.

Figure 6.7 shows the cost function for the DSMC simulation with $Kn_s = 0.005$ and l for 3.0, 4.5 and 7.5mm. The cost functions are constant until a certain d_{shock} at which

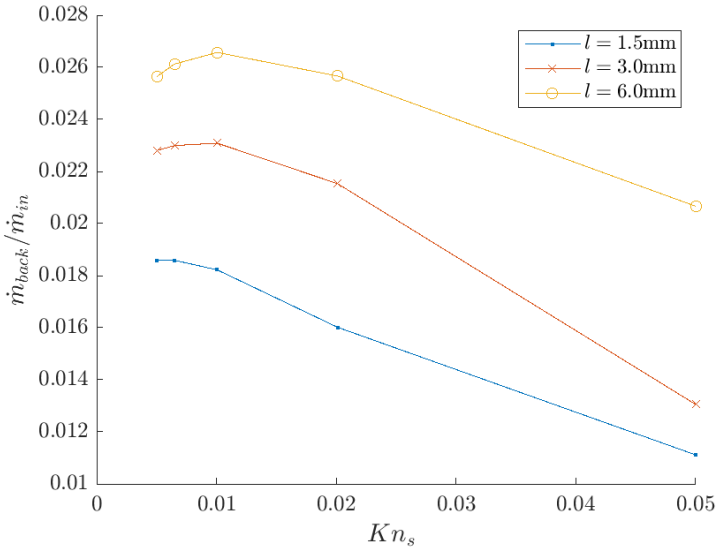

Figure 6.6: The relative back flow rate, for different inlet condition Kn_s and distance between jets l.

the shock leaves the line $y = l$, as $\dot{m}_{pen}$ is zero. Therefore, the cost function can be approximated by $\frac{m_{in}}{l}$ for $d < d_{shock}$ when a shock occurs. If there is no shock, then $\frac{m_{in}}{l}$ is only accurate for $d \approx 0$mm. The cost function is therefor bounded by

$$\frac{m_{in}}{l} \geq c\,(0, l, Kn_s) \geq c\,(d, l, Kn_s)\,. \tag{6.7}$$

The upper limit is proportional to $\frac{1}{Kn}\frac{1}{l}$. Furthermore, figure 6.7 shows that for $d > d_{shock}$ the cost function is higher for larger l, which agrees with the results for the density (figure 5.21). The higher cost function for larger l is not observed for gas flow without a shock (figure 6.8).

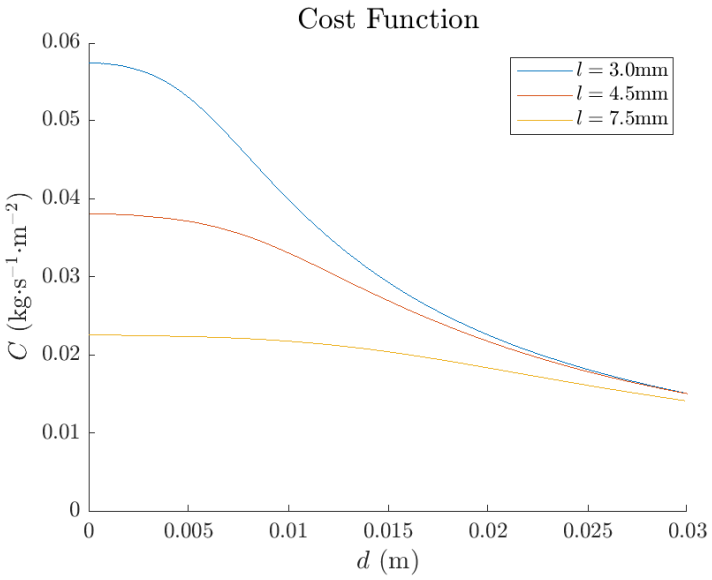

Figure 6.8: The cost function c depending on the position of the sheet d, for $Kn_s = 0.05$.

6.2. CONSTRAINT

A coating is in practice not uniformly applied to the sheet. This uniformity is quantified by the surface roughness R_a, which can be calculated by the relative difference in thickness h_i compared to the average, for multiple points i, by[18]

$$R_a = \frac{1}{n}\sum_{i=1}^{n} |h_i|. \tag{6.8}$$

In our case the roughness depends on the thickness of the coating. Therefore, we introduce the relative roughness r_a, which is defined by

$$r_a = \frac{1}{\dot{m}_{coat}} \int_0^l |\rho V_x - \dot{m}_{coat}| \mathrm{d}y. \tag{6.9}$$

The relative roughness in this thesis is only used to describe the uniformity of the vapor deposition. The measured roughness of a sheet of metal also depends on other aspects such as surface diffusion, which are not discussed in this thesis. There are different methods for defining the roughness. We use the arithmetic average, which does not depend on small statistical errors. The constraint is to have a relative roughness below a certain number, i.e.

$$r_a(d, l, Kn_s) \leq r_{a,max}. \tag{6.10}$$

The relative roughness for different $Kn_s = 0.005$ simulations is shown in figure 6.9. At $d = 0$, the mass flow is concentrated at the inlet combined with the back flow, results in high uniformity. The gas expands, which distributes the mass flow thereby lowering r_a. This continues until the shock results in a rise. The shock then moves to the boundary of

the sheet at which r_a start to decrease slowly as the entire shock is outside the roughness domain. The roughness is usually lower for smaller l and is only higher at the bump. Comparing these results with figure 6.10, shows again that the roughness is lower for smaller l. However, for $Kn_s = 0.05$ there is no shock and the roughness is consequently smaller for the whole domain.

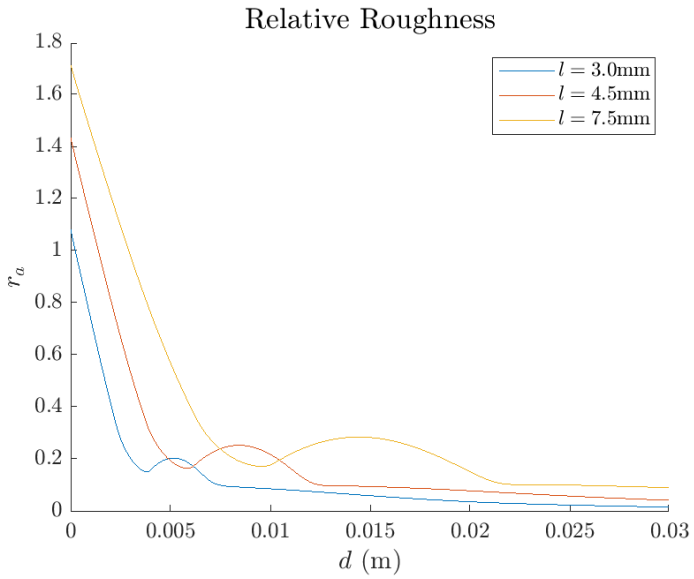

Figure 6.9: The relative roughness r_a depending on the position of the sheet d, for $Kn_s = 0.005$.

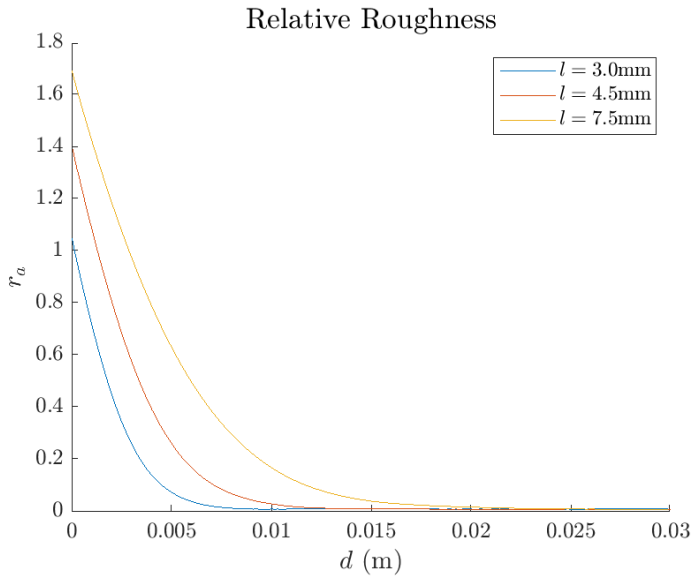

Figure 6.10: The relative roughness r_a depending on the position of the sheet d, for $Kn_s = 0.05$.

The roughness shows similarity depending on d. Comparing the roughness with each other, the same way as was done for the penetration mass flow $\dot{m}_{pen}$, shows the same correlation. However, for $d = 0$ and at the bump the difference is significant. This difference for small d is outside the optimization domain and thus irrelevant. The difference caused by the bump is significant but for small difference between l_1 and l_2, the approximation

$$r_a(d, l_1) \approx r_a\left(d\frac{l_2 - b}{l_1 - b}, l_2\right) \tag{6.11}$$

still holds. A better option is to use this approximation for a linear progression between two simulations. For $Kn_s = 0.05$ in figure 6.12, the approximation also holds.

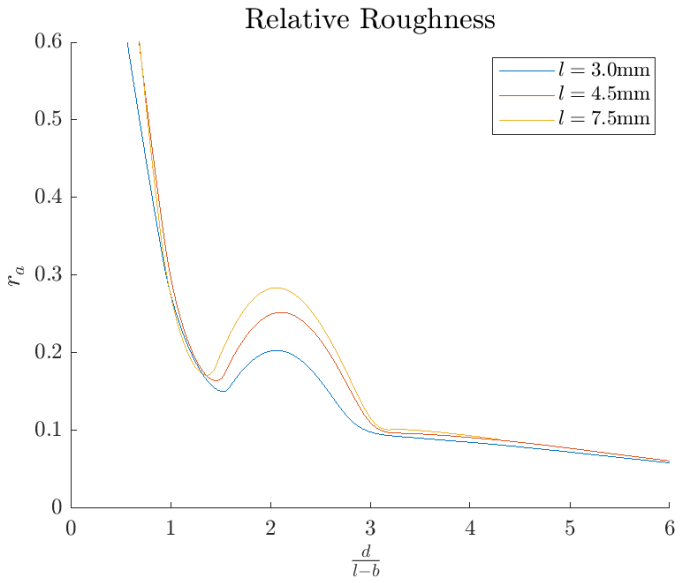

Figure 6.11: The relative roughness r_a depending on $\frac{d}{l-b}$ with $b = 0.5$mm, for $Kn_s = 0.005$.

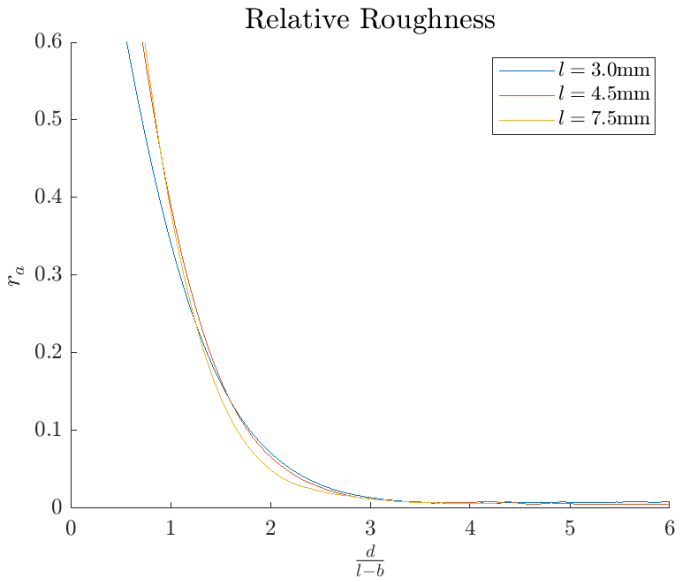

Figure 6.12: The relative roughness r_a depending on $\frac{d}{l-b}$ with $b = 0.5$mm, for $Kn_s = 0.05$.

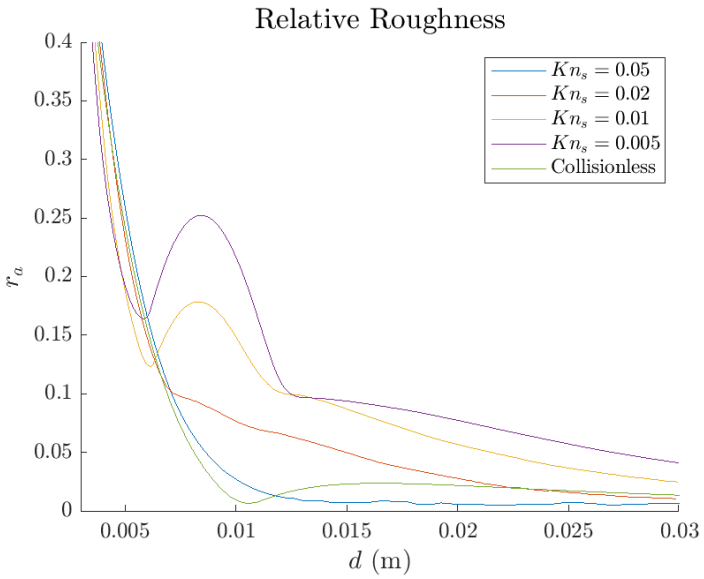

Figure 6.13: The relative roughness r_a depending on the position of the sheet d, for $l = 3.0$mm.

The roughness changes for different Kn_s. Figure 6.13 shows, the roughness to be smaller for larger Kn_s. The roughness for $Kn_s = 0.05$ is general the lowest and is even lower compared to the collisionless case. It is even lower as in figure 6.13, as the statistical error starts to influence its value.

6.3. RESULTS

For the optimiziaton problem:
Find d, l, Kn_s to

$$\begin{aligned} &\text{maximize} && c(d,l,Kn_s) \\ &\text{subject to} && r_a \leq r_{a,max} \\ & && 10\text{mm} \leq d \leq 30\text{mm}, \\ & && 3.0\text{mm} \leq l \leq 7.5\text{mm}, \\ & && 0.005 \leq Kn_s \leq 0.05, \end{aligned}$$

with,

$$c(d,l,Kn_s) = \frac{\int_0^l \rho V \mathrm{d}y}{l} \tag{6.12}$$

and $r_{a,max} = \infty$, gives the optimal solution at $Kn_s = 0.005$, as smaller Kn_s will always result in a higher cost function. This is because, the effect of Kn_s on the total mass flow is sufficiently larger compared to the change in the interaction effect. The optimum is at $d = 10$mm, as the cost function is a strictly decreasing function. However, the optimal is not expected to be on the boundary. This follows from figure 6.7, the maximum of the cost function for $l = 3.0$mm is not contained in the domain of the optimization and the cost function is not larger for the whole domain. Using the approximation 5.1 with $b = 0.5$mm, gives an estimation of the cost function for a range of l. Figure 6.14 shows

the approximated cost functions for the cases l = 3.0mm and l = 4.5mm, which show a significant difference. The average and linear progression are also shown. These lines should give a better estimate between these points.

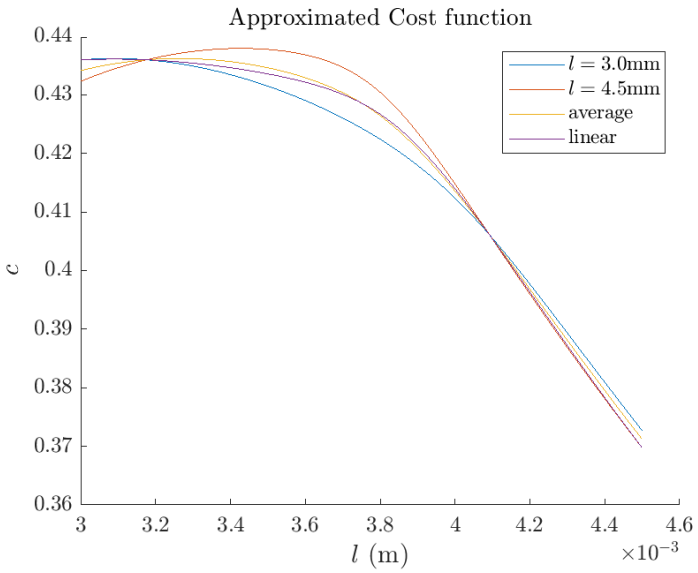

Figure 6.14: The approximated cost function by using the data from l = 3.0mm and l = 4.5mm using b = 0.5mm. The approximation is done for both simulations, the average and linear progression. With Kn_s = 0.005 and d = 10mm

These results can be used in a line search, in which each step gives a value for l closer to the optimum. These approximations used a constant value for b, which can be improved by using a calculated function $b(d)$, for which two simulations are needed. This approximation is compared to simulation in figure 6.15. It shows that the approximation is sufficiently close.

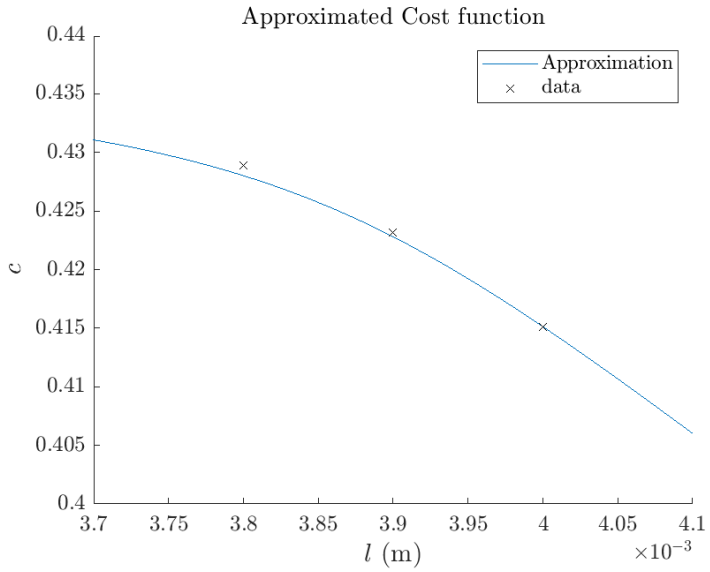

Figure 6.15: The approximated cost function with b depending on d. Compared with data

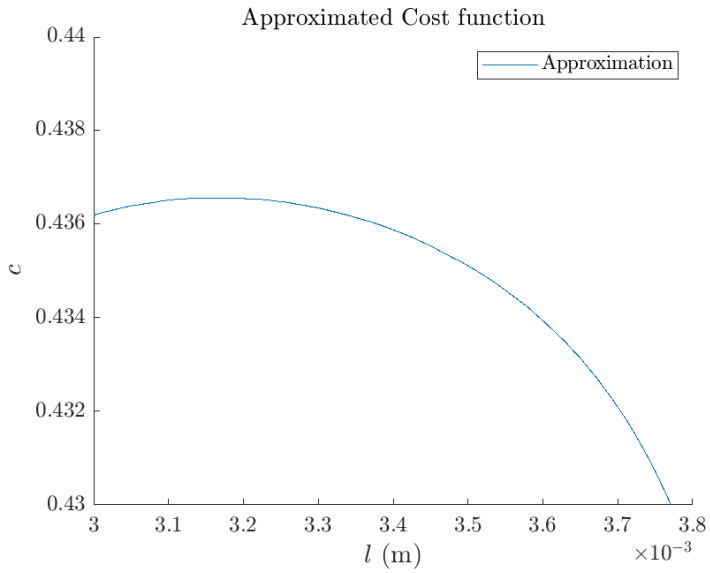

Figure 6.16: The approximated cost function with an optimum at $l = 3.17$.

Using a closer points, the optimum is approximated to be at $l = 3.17$mm with the optimum $c = 0.4363$, as shown in figure 6.16. The optimum has a relative roughness of $r_{a,opt} = 0.0887$. If $r_{a,opt} \leq r_{a,max}$ then the roughness constraint does not influence the

optimum. This is lower than the roughness at the shock regime. Therefore, the approximation for the roughness can be used for all Kn_s as the regime for which the approximation does not hold within the region of interest. For lower $r_{a,max}$, the roughness starts to play a role. The roughness can be approximated similarly to the penetration mass flow. This results in an estimate without doing multiple simulations. Taking $r_{a,max}$ just below $r_{a,opt}$, the optimum should be close to the previous optimum. The direction of the new position is found by using the partial derivatives for the cost function and the relative roughness. The ratios

$$\frac{\partial c}{\partial d}\left(\frac{\partial r_a}{\partial d}\right)^{-1}, \tag{6.13a}$$

$$\frac{\partial c}{\partial l}\left(\frac{\partial r_a}{\partial l}\right)^{-1}, \tag{6.13b}$$

$$\frac{\partial c}{\partial [Kn_s]}\left(\frac{\partial r_a}{\partial [Kn_s]}\right)^{-1} \tag{6.13c}$$

(6.13d)

give the change of the cost function given by the change in relative roughness. A high ratio means big change in cost function compared to the roughness. The ratio for l is the smallest. Therefore the new optimum would again be at the line $Kn_s = 0.005$, $d = 10$mm. The roughness at $d = 10$mm, $l = 3.0$mm and $Kn_s = 0.005$ is 0.0850. For $0.0887 < r_{a,max} < 0.0850$, the optimization is a one dimensional optimization in the l-direction given by:

Find l to
maximize $c(l)$
subject to $r_a \leq r_{a,max}$
$3.0\text{mm} \leq l \leq 7.5\text{mm}$.

This can be solved using a line search. For $r_{a,max} = 0.085$, the optimum is found at $d = 10$mm, $l = 3.0$mm and $Kn_s = 0.005$. The ratios of partial derivatives is still smallest for l. However, l is bounded by the domain. Therefore, the optimum will be on the line, $l = 3.0$mm and $Kn_s = 0.005$. This gives a one-dimensional optimization problem in the d-direction, for $0.085 < r_{a,max} < 0.0148$. just below 0.0148, it becomes a one-dimensional optimization problem in the Kn_s-direction. The optimum depending on the relative roughness is shown in figure 6.17.

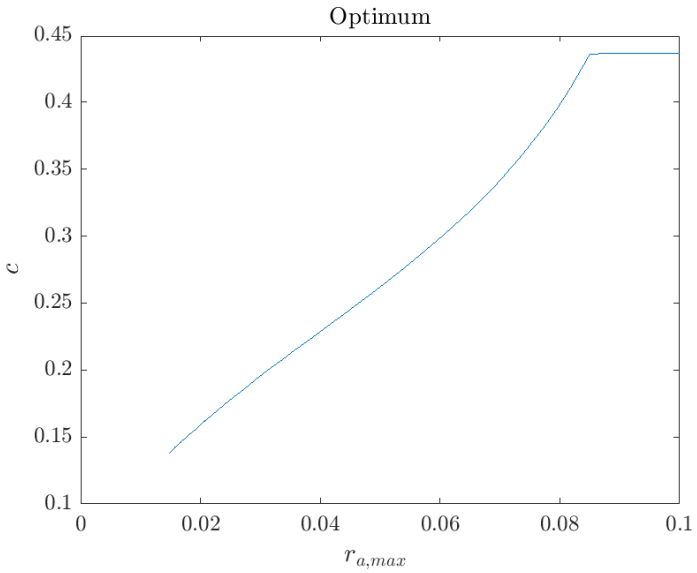

Figure 6.17: The optimal cost function depending on the limiter $r_{a,max}$.

6.4. GRADIENT DESCENT

One way to find an optimum is by using the gradient descent algorithm [13]. It utilises the gradient of the cost function $\nabla c(\boldsymbol{x}_i)$ for point $\boldsymbol{x}_i$ to find the next point $\boldsymbol{x}_{i+1}$ in a sequence $(\boldsymbol{x}_n)_{n\in\mathbb{N}}$, which leads to a local optimum. Different methods can be applied to find the next point $\boldsymbol{x}_{i+1}$ by tuning the direction and size of the next step.
This method uses the gradients of the cost function and constraints to find the next point $\boldsymbol{x}_i$. However, the cost function is bounded proportional to $1/l$ and $1/Kn_s$. Therefore, it is easier to use

$$\boldsymbol{x} = \begin{bmatrix} x_d \\ x_l \\ x_{Kn} \end{bmatrix} = \begin{bmatrix} \frac{1}{d} \\ \frac{1}{l} \\ \frac{1}{Kn_s} \end{bmatrix}, \tag{6.14}$$

as this gives a linear dependence. The gradient can be approximated using the Taylor series. The first order Taylor series approximates the derivative of the cost function with respect to a vector $\boldsymbol{r}$ by

$$\frac{\partial c}{\partial \hat{\boldsymbol{r}}} = \frac{c(\boldsymbol{x}+\boldsymbol{r}) - c(\boldsymbol{x})}{|\boldsymbol{r}|} + \mathcal{O}(|\boldsymbol{r}|). \tag{6.15}$$

Taking $\boldsymbol{r}$ as a small distance in the x_i-direction gives

$$\frac{\partial c}{\partial x_i} \approx \frac{c(\boldsymbol{x}+h\hat{x}_i) - c(\boldsymbol{x})}{h}. \tag{6.16}$$

The partial derivative for x_d follows from the simulation. Therefore, two additional simulations must be done to get the gradient with this method. The gradient can also be approximated by using

$$\nabla c = \begin{bmatrix} \frac{\partial c}{\partial x_d} \\ \frac{\partial c}{\partial x_l} \\ \frac{\partial c}{\partial x_{Kn}} \end{bmatrix} = \begin{bmatrix} \frac{\partial [x_l(\dot{m}_{in} - \dot{m}_{pen})]}{\partial x_d} \\ \frac{\partial [x_l(\dot{m}_{in} - \dot{m}_{pen})]}{\partial x_l} \\ \frac{\partial [x_l(\dot{m}_{in} - \dot{m}_{pen})]}{\partial x_{Kn}} \end{bmatrix} = \begin{bmatrix} -x_l \frac{\partial \dot{m}_{pen}}{\partial x_d} \\ \frac{x_d(x_l+b)}{x_l} \frac{\partial \dot{m}_{pen}}{\partial x_d} + \dot{m}_{in} - \dot{m}_{pen} \\ x_l \frac{\partial (\dot{m}_{in} - \dot{m}_{pen})}{\partial x_{Kn}} \end{bmatrix}. \quad (6.17)$$

Here we use the approximation for $\frac{\partial \dot{m}_{pen}}{\partial x_l} = -\frac{x_d(x_l+b)}{x_l^2} \frac{\partial \dot{m}_{pen}}{\partial x_d}$, which results from equation 5.1. The partial derivative with respect to x_d is given by the simulation. The partial derivative for x_{Kn} is unknown and can be approximated using the Taylor series. This method uses one additional simulation to estimate the gradient.
However, approximating the cost function and roughness uses fewer simulations than both gradient descent methods. The approximation gives a rough estimation for the entire range of l and has no significant difference for nearby l. Using this to do a line search is thereby in general faster than a gradient descent over the line l. These findings can be useful for future problems. If all constraints can be approximated for different l, then the optimum can be found with fewer simulations compared to gradient descent.

7

CONCLUSIONS

The purpose of the current study was to determine the interaction effect between two rarefied two-dimensional vapor jets in vacuum. The aim was to observe different regimes and in particular the one with a shock. For this purpose, we derived the analytical solution for the collisionless case to determine the difference caused by the interaction effect. Furthermore, we wanted to know how the interaction effect depends on the stagnation Knudsen number Kn_s and the distance between jets l. Additionally, we studied how to optimize the mass flow for coating using these parameters.
The macroscopic properties have a statistical error, which is influenced by the time step. The autocorrelation in a cell depends on the macroscopic properties and the properties and position of the cell. Larger cells result in general in a longer autocorrelation time.
The analytical solution is found to match the collisionless DSMC results for both the single jet and the dual jets. However, the density field of a solo jet is not equal to the analytical solution below a certain Kn_s value. Therefore, the analytical solution should not be used as a single jet approximation to observe the effect of a second jet. Furthermore, the analytical solution should not be used to estimate the penetration Knudsen number as a better method was found. However, the derivative of the equations can be used in combination with a single jet simulation, to generate a interactionless comparison.
A dual jets simulation with a stagnation Knudsen number of 0.0065 results in a shock wave, which is caused by a secondary jet resulted from the interaction. This secondary jet splits the density, which causes uniformity for physical vapor deposition. Additionally, the shock protects the jet from particles of the other jet, in the region before the shock. This region is therefore unaffected by the other jet and thus equal to the single jet, which can be used for calculating the penetration Knudsen number.
There are different interaction effects depending on the stagnation Knudsen number Kn_s which is inversely proportional to the inlet density. For $Kn_s \approx 0.05$, the interaction effect is small and is similar to the collisionless case. However, there is a small interaction effect, which causes the density between the jets to be higher compared to a collisionless effect. Lower Kn_s around 0.02, shows a noticeable effect on the density field. However, there is no shock. Simulation with Kn_s below 0.01 showed a shock, which is steeper for

smaller Kn_s.
The distance between inlets l also changes the interaction effect. For l much smaller than the width of the inlet h, the interaction effect can be neglected and the macroscopic properties are similar to that of a single larger jet. This contradicts with the penetration Knudsen number, which expected a larger interaction effect. Comparing larger l, shows no difference, apart from a further position of the shock and lower density for larger distance between inlets. Noticeable is the lower density at the axis of the inlet after the shock, for smaller l.
The optimization resulted to be optimal for smallest distance l between jets, for which the relative mass flow increases and the uniformity decreases. However, this changes after the shock leaves the mass flow region. Then larger distances between inlet have a higher cost value. The optimal value for l is thus where the shock leaves the mass flow region, which is for $l = 3.17$mm at 10mm. For the optimization it is shown, that the mass flow rate and constrained can be approximated for different l, which is accurate for small difference. This gives a good estimation where the optimal resides, and is thus useful for a line search. The similarity is also useful in the gradient descent methods, to calculate a partial derivative, which is otherwise approximated. This reduces the number of required simulations.

8

RECOMMENDATIONS

More research is needed to better understand the interaction effect. How do the inlet temperature and inlet velocity influence the interaction effect. The temperature influences the inlet velocity fluctuations in all directions. This could influence the interaction effect as it would result in higher relative speed for the particles between the jets. It would be interesting to assess diatomic gas, as this gives another energy reservoir, which may change the behavior.
A better parameter is required to describe the interaction effect, which could be done by taking the size of the inlet into account. The ratio between the size inlet and gap between inlet is expected to influence the interaction.
Further research could look at the interaction effect at higher densities cases. However, these have a high computational cost with the Direct Simulation Monte Carlo method. Therefore, continuum mechanics should be used. These higher densities cases could help us understand the limit of the interaction effect.
The similarity found for the penetration mass flow for different length between inlets could depend on the velocity of the gas flow. Whether this is true should be studied. Understanding this similarity can help us understand the interaction effect. A more accurate approximation of the penetration mass flow can also be used for similar optimization problems.
Further research in vapor deposition with multiple jets shows the interaction effect between two shock wave. This can be done by using two symmetry boundaries. Since the studied Physical Vapor Deposition apparatus will have multiple nozzles, this problem seems to be worth studying.
This research could also be validated by experimental results. Hover, it is expected to be technically challenging to manufacture two long slits with homogeneous inlet conditions.

A

Analytic Solution Single Jet

The analytical solution for the two-dimensional solo jet expansion in vacuum is given below. These solutions calculate the properties in the x,y-domain. The number density and velocity where solved and validated by Chumpei and Boyd[3]. The temperature was solved and validated by Khasawneh, Liu and Cai[8]. These formulas use two angles θ_1 and θ_2. These angles are the angles at the two end points of the inlet. They are calculated with the inverse tangent by

$$\theta_1 = \tan^{-1}\left(\frac{y-h/2}{x}\right),$$
$$\theta_2 = \tan^{-1}\left(\frac{y+h/2}{x}\right).$$

Here h stands for the size of the inlet. The analytical solution also depend on the specific plume exiting speed $S_0 = U_0\sqrt{\frac{m}{2kT_0}}$, where U_0 stands for the inlet speed, T_0 for the inlet temperature, m the mass of one particle and k the Boltzmann constant. Using U_0 and the angles θ_1, θ_2 the equation for the number density is given by

$$\begin{aligned} n(x,y) = &\frac{\exp\left(-S_0^2\right)}{2\pi}(\theta_2-\theta_1) + \frac{1}{4}\left[\operatorname{erf}(S_0\sin\theta_2) - \operatorname{erf}(S_0\sin\theta_1)\right] \\ &+ \frac{S_0}{2\sqrt{\pi}}\int_{\theta_1}^{\theta_2}\exp\left(-S_0^2\sin^2\theta\right)\operatorname{erf}(S_0\cos\theta)\,\mathrm{d}\theta. \end{aligned} \tag{A.2}$$

The velocity of the gas flow is different depending on the direction. Therefore, V_x and V_y are calculated independently with

$$\begin{aligned} V_x(x,y) = &\sqrt{\frac{2kT_0}{m}}\frac{\exp\left(-S_0^2\right)}{2n\pi}\left(\frac{S_0(\theta_2-\theta_1)}{2} + \frac{S_0\left[\sin(2\theta_2)-\sin(2\theta_1)\right]}{4}\right. \\ &\left.+\sqrt{\pi}\int_{\theta_1}^{\theta_2}\left[\left(\frac{1}{2}\cos\theta + S_0^2\cos^3\theta\right)\left[1+\operatorname{erf}(S_0\cos\theta)\right]\exp\left(S_0^2\cos^2\theta\right)\right]\mathrm{d}\theta\right), \end{aligned} \tag{A.3}$$

$$V_y(x,y) = \sqrt{\frac{2kT_0}{m}}\frac{1}{4\sqrt{\pi}n}\Big(\exp\left(-S_0^2\sin^2\theta_1\right)\cos\theta_1\left[1+\operatorname{erf}\left(S_0\cos\theta_1\right)\right] - \exp\left(-S_0^2\sin^2\theta_2\right)\cos\theta_2\left[1+\operatorname{erf}\left(S_0\cos\theta_2\right)\right]\Big). \tag{A.4}$$

Both equations depend on the number density $n(x,y)$.
The temperature of the gas is calculated by

$$T(x,y) = -\frac{V_x^2+V_y^2}{3}\frac{m}{k} + e_T. \tag{A.5}$$

With e_T the part that corresponds to the total energy which is expressed by

$$e_T = \frac{T_0\exp\left(-S_0^2\right)}{6\pi n}\left[3\Delta\theta + S_0^2\left(\Delta\theta + \frac{1}{2}\left[\sin\left(2\theta_2\right) - \sin\left(2\theta_2\right)\right]\right) + 2S_0\sqrt{\pi}\int_{\theta_1}^{\theta_2}\left(2\cos\theta + S_0^2\cos^3\theta\right)\exp\left(S_0^2\cos^2\theta\right)\left[1+\operatorname{erf}\left(S_0\cos\theta\right)\right]\mathrm{d}\theta\right]. \tag{A.6}$$

The equation for T is split as for calculating the analytical solution for the dual jets is calculated by using e_T and not T. The equations for the properties are all symmetric over the line $x = 0$.

B

Flow Field Results

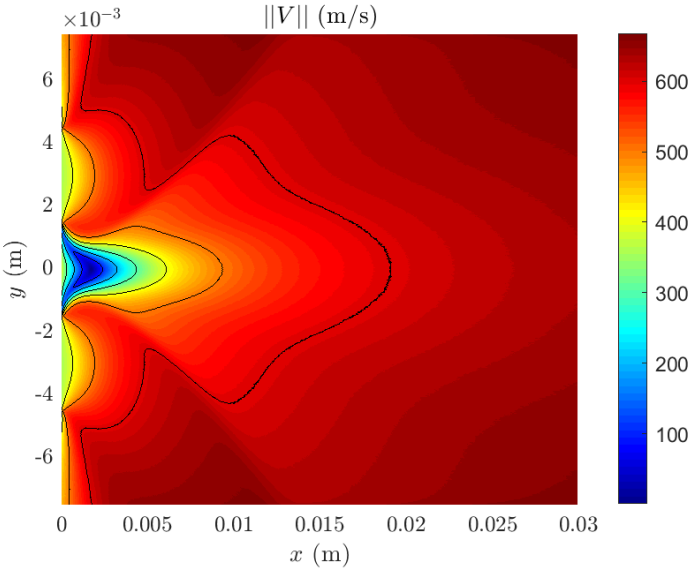

Figure B.1: Contours of the magnitude of the velocity for two interacting jets with inlet condition $Kn_s = 0.0065$ and separation distance $l = 3.0$mm.

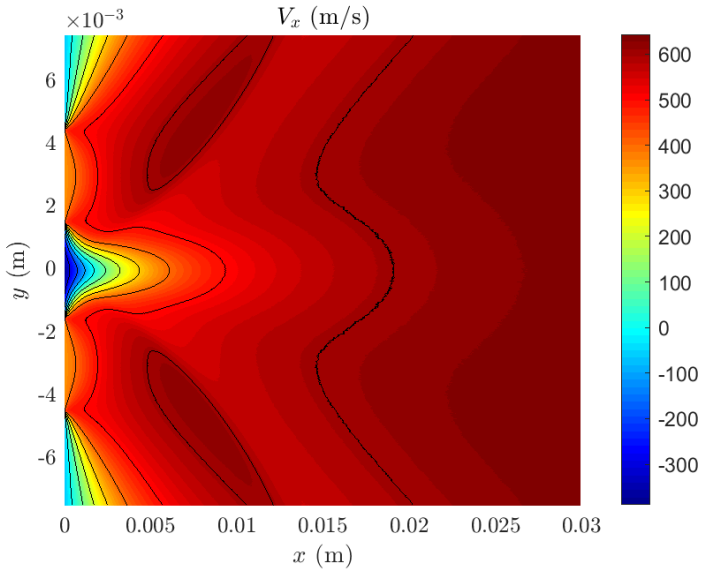

Figure B.2: Contours of the velocity V_x for two interacting jets with inlet condition $Kn_s = 0.0065$ and separation distance $l = 3.0$mm.

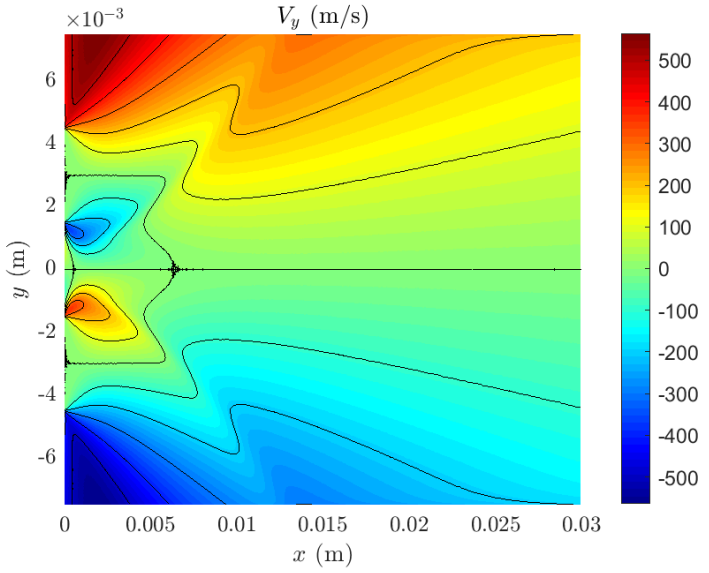

Figure B.3: Contours of the velocity V_x for two interacting jets with inlet condition $Kn_s = 0.0065$ and separation distance $l = 3.0$mm.

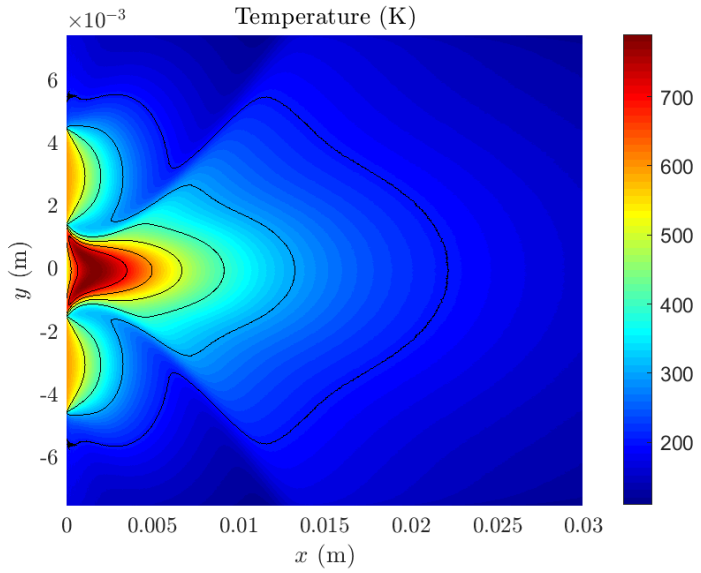

Figure B.4: Contours of the temperature for two interacting jets with inlet condition $Kn_s = 0.0065$ and separation distance $l = 3.0$mm.

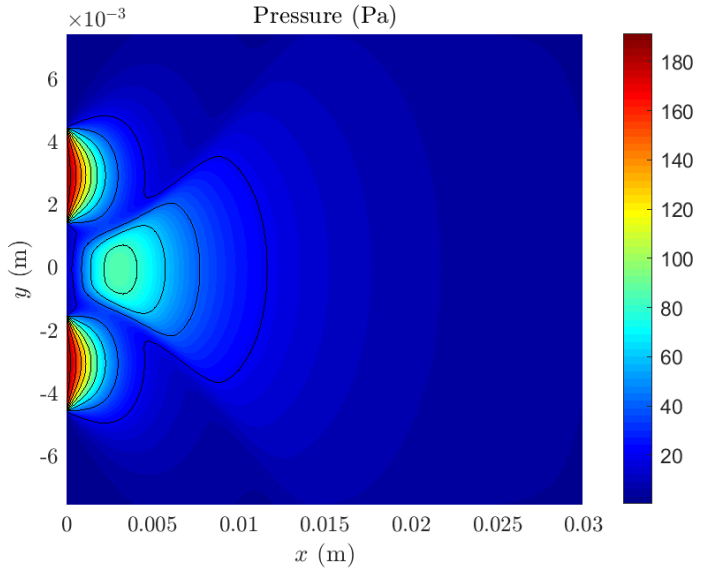

Figure B.5: Contours of the pressure for two interacting jets with inlet condition $Kn_s = 0.0065$ and separation distance $l = 3.0$mm.

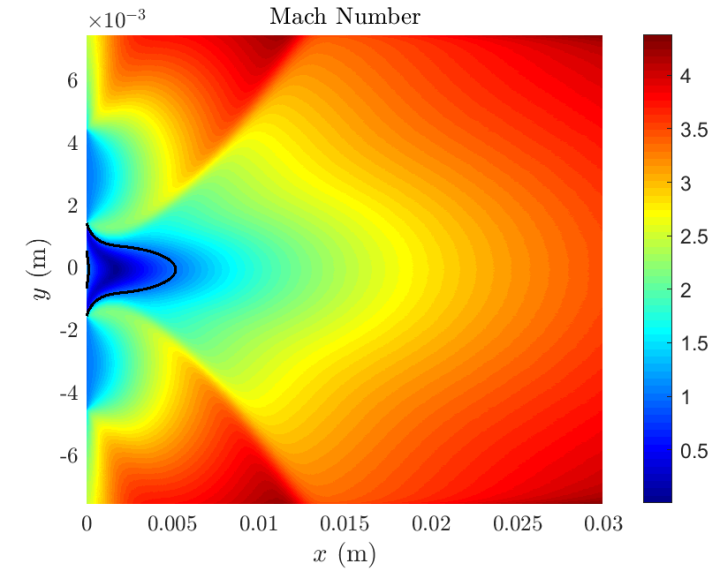

Figure B.6: Contours of Mach number for two interacting jets with inlet condition $Kn_s = 0.0065$ and separation distance $l = 3.0$mm, with the black line at $M = 1$, dividing subsonic and supersonic.

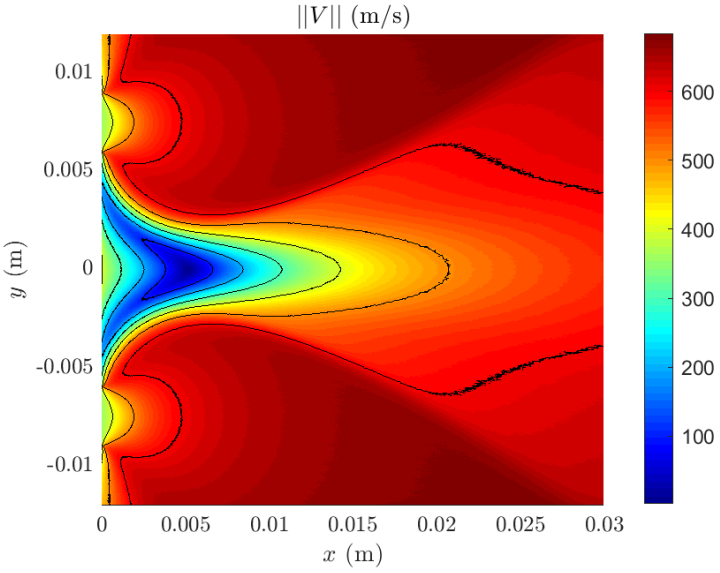

Figure B.7: Contours of the magnitude of the velocity for two interacting jets with inlet condition $Kn_s = 0.0065$ and separation distance $l = 7.5$mm.

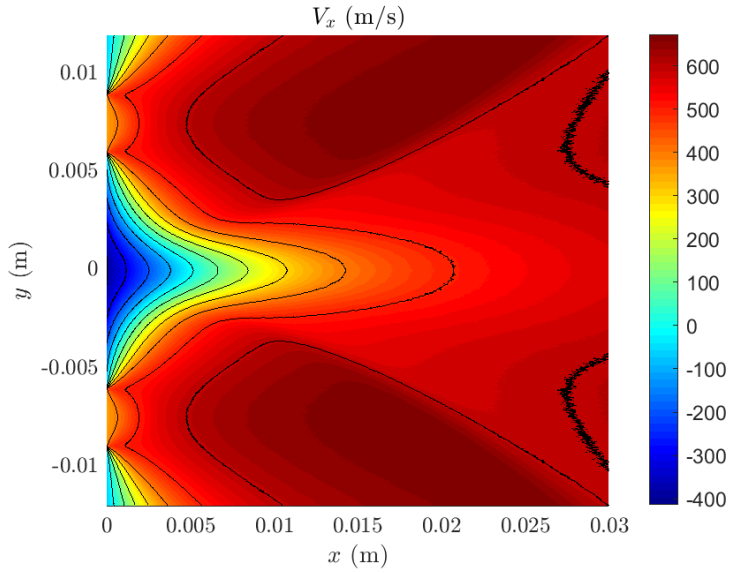

Figure B.8: Contours of the velocity V_x for two interacting jets with inlet condition $Kn_s = 0.0065$ and separation distance $l = 7.5$mm.

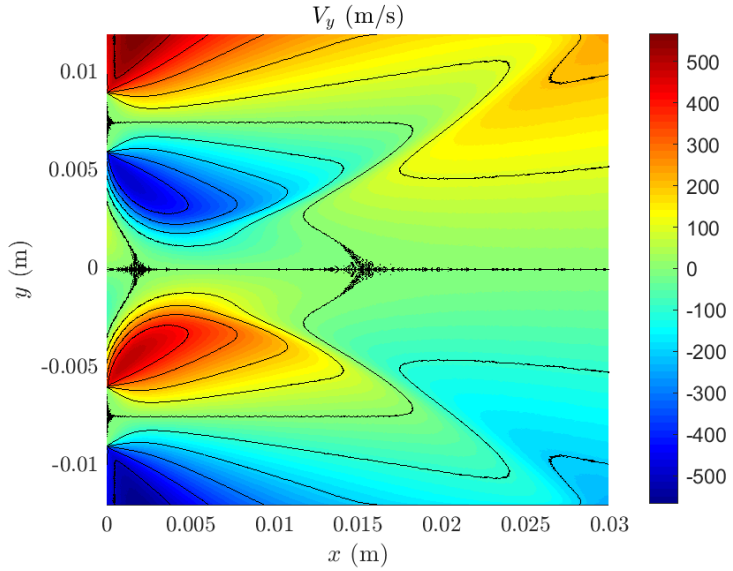

Figure B.9: Contours of the velocity V_x for two interacting jets with inlet condition $Kn_s = 0.0065$ and separation distance $l = 7.5$mm.

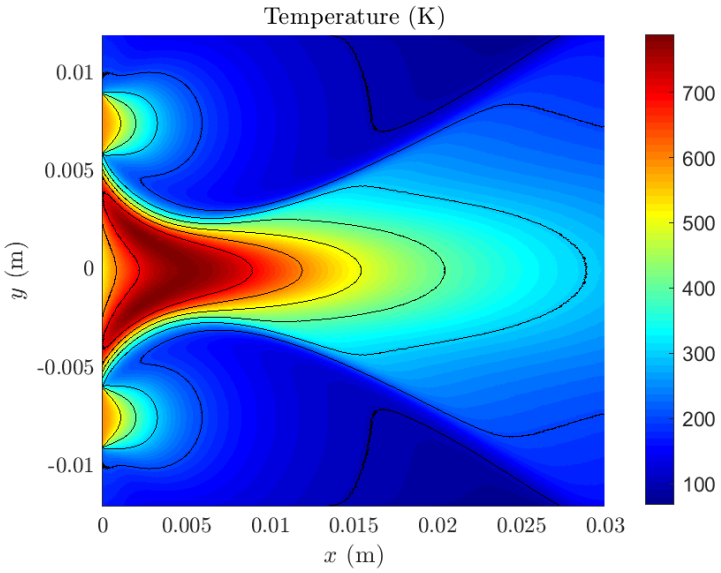

Figure B.10: Contours of the temperature for two interacting jets with inlet condition $Kn_s = 0.0065$ and separation distance $l = 7.5$mm.

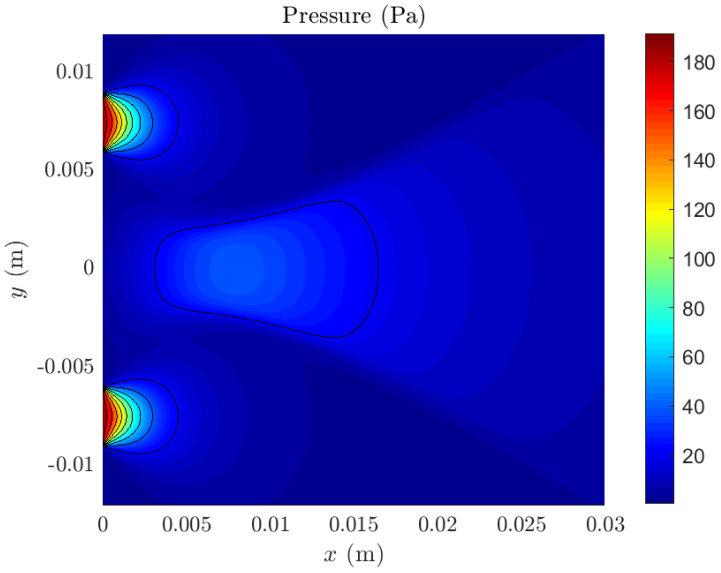

Figure B.11: Contours of the pressure for two interacting jets with inlet condition $Kn_s = 0.0065$ and separation distance $l = 7.5$mm.

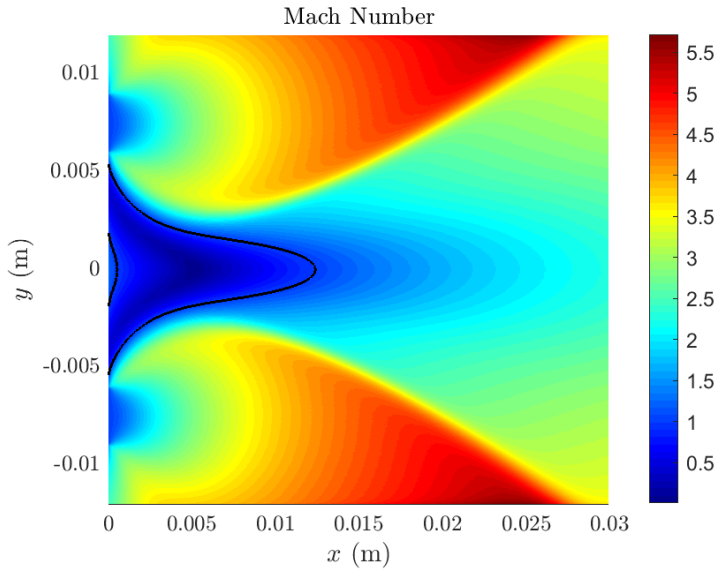

Figure B.12: Contours of Mach number for two interacting jets with inlet condition $Kn_s = 0.0065$ and separation distance $l = 7.5$mm, with the black line at $M = 1$, dividing subsonic and supersonic.

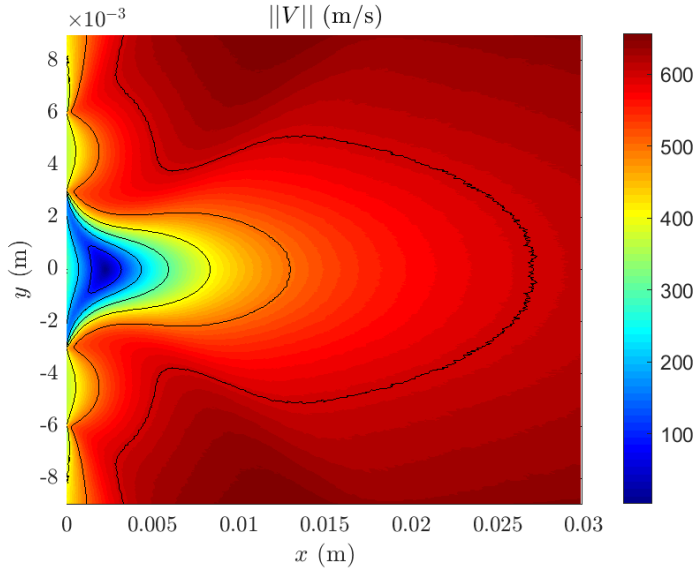

Figure B.13: Contours of the magnitude of the velocity for two interacting jets with inlet condition $Kn_s = 0.02$ and separation distance $l = 4.5$mm.

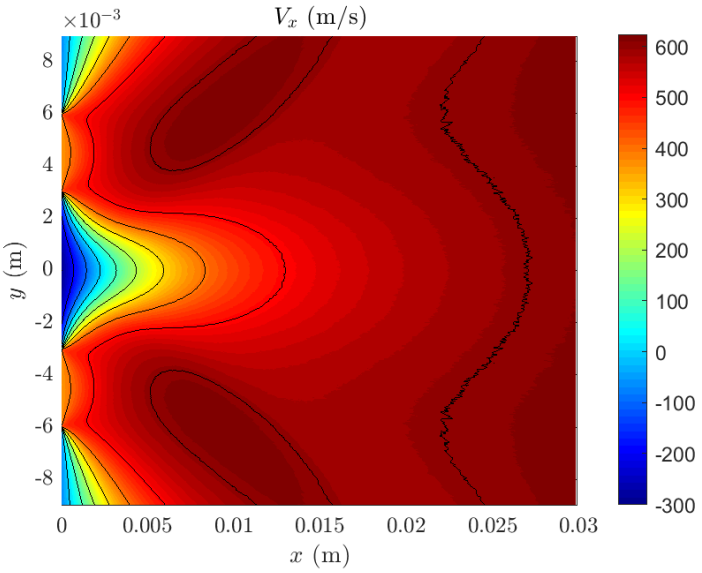

Figure B.14: Contours of the velocity V_x for two interacting jets with inlet condition $Kn_s = 0.02$ and separation distance $l = 4.5$mm.

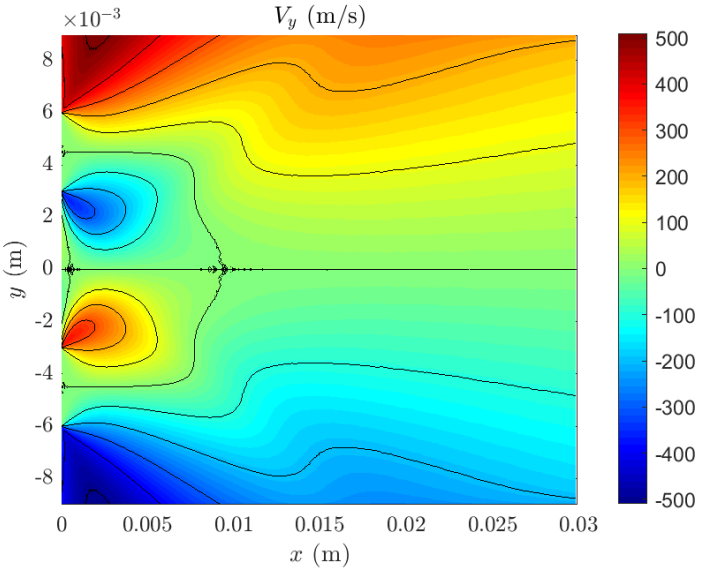

Figure B.15: Contours of the velocity V_x for two interacting jets with inlet condition $Kn_s = 0.02$ and separation distance $l = 4.5$mm.

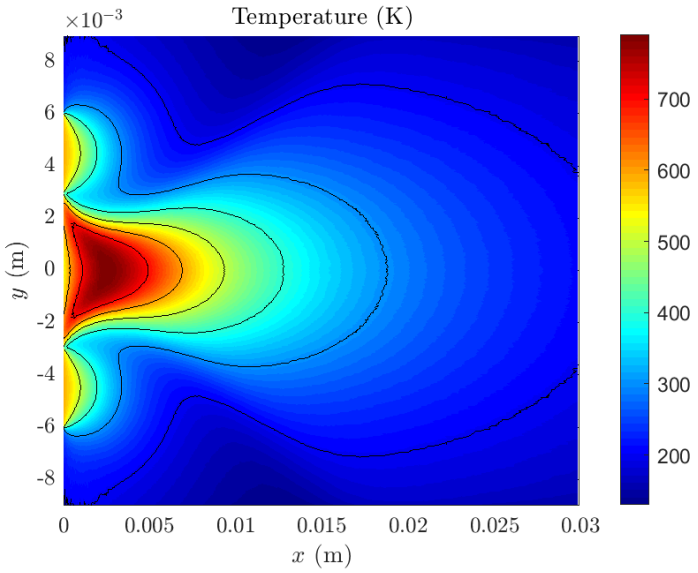

Figure B.16: Contours of the temperature for two interacting jets with inlet condition $Kn_s = 0.02$ and separation distance $l = 4.5$mm.

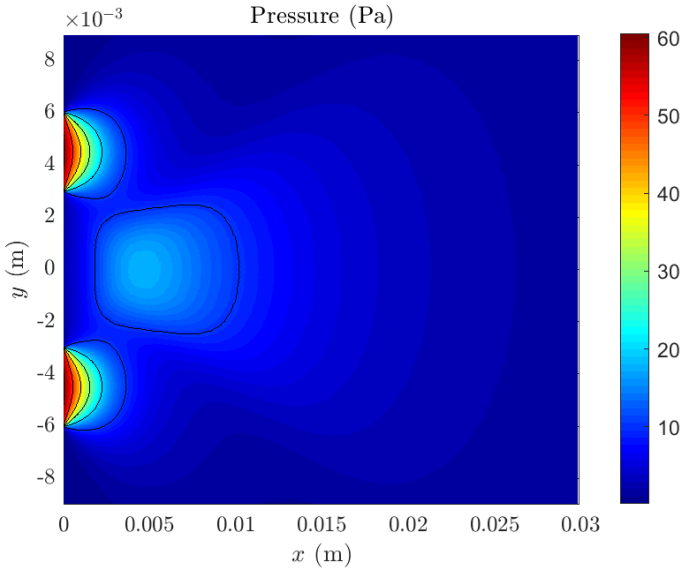

Figure B.17: Contours of the pressure for two interacting jets with inlet condition $Kn_s = 0.02$ and separation distance $l = 4.5$mm.

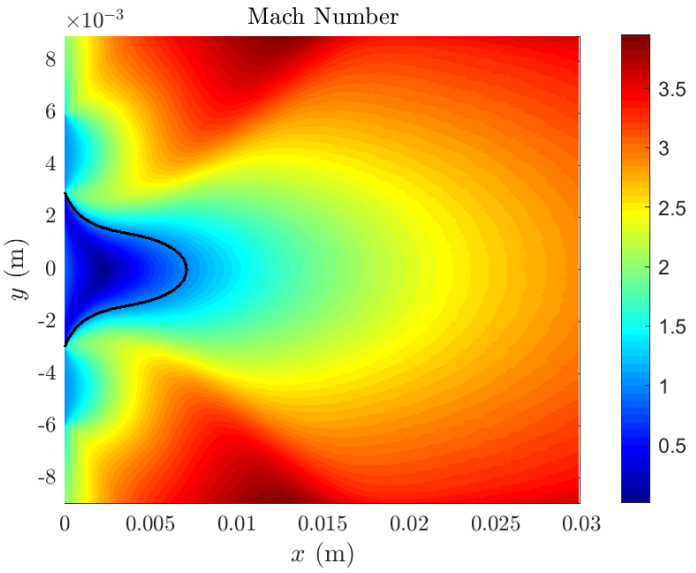

Figure B.18: Contours of Mach number for two interacting jets with inlet condition $Kn_s = 0.02$ and separation distance $l = 4.5$mm, with the black line at $M = 1$, dividing subsonic and supersonic.

BIBLIOGRAPHY

REFERENCES

[1] Christine Ahner, Peter Maaß, and Peter Peißker. *Handbook of hot-dip galvanization*. John Wiley & Sons, 2011.

[2] G.A. Bird. *Molecular Gas Dynamics and the Direct Simulation of Gas Flows*. Number v. 1 in Molecular Gas Dynamics and the Direct Simulation of Gas Flows. Clarendon Press, 1994. ISBN 9780198561958.

[3] Cai C. and Boyd I. Theoretical and numerical study of several free molecular flow problems. *J. Spacecr. Rockets*, 44:619, 2007.

[4] Ivan A Chirokov, Tatiana G Elizarova, Jean-Claude Lengrand, Isabelle Gibek, and Irina A Graur. Experimental and numerical investigation of rarefied interacting plumes. In *AIP Conference Proceedings*, volume 663, pages 572–579. AIP, 2003.

[5] D. J. Economou, T. J. Bartel, R. S. Wise, and D. P. Lymberopoulos. Two-dimensional direct simulation monte carlo (dsmc) of reactive neutral and ion flow in a high density plasma reactor. *IEEE Transactions on Plasma Science*, 23(4):581–590, Aug 1995. ISSN 0093-3813. doi: 10.1109/27.467978.

[6] Martin Grabe, Georg Dettleff, and Klaus Hannemann. Impact of nozzle separation on the plumes of two parallel thrusters. In *AIP Conference Proceedings*, volume 1786, page 170005. AIP Publishing, 2016.

[7] André Holz, Georg Dettleff, Klaus Hannemann, and Stefan Ziegenhagen. Experimental investigation of two interacting thruster-plumes downstream of the nozzles. *Space Propulsion*, 2012.

[8] Khaleel Khasawneh, Hongli Liu, and Chunpei Cai. Highly rarefied two-dimensional jet impingement on a flat plate. *Physics of Fluids*, 22(11):117101, 2010.

[9] Wenhai Li. *Analysis of Single and Dual Under-Expanded, Rarefied Jets*. PhD thesis, The Graduate School, Stony Brook University: Stony Brook, NY., 2010.

[10] W. W. Liou and Y. Fang. Heat transfer in microchannel devices using dsmc. *Journal of Microelectromechanical Systems*, 10(2):274–279, June 2001. ISSN 1057-7157. doi: 10.1109/84.925780.

[11] Donald M Mattox. *Handbook of physical vapor deposition (PVD) processing*. William Andrew, 2010.

[12] Roddam Narasimha. Collisionless expansion of gases into vacuum. *Journal of Fluid Mechanics*, 12(2):294–308, 1962. doi: 10.1017/S0022112062000208.

[13] Jorge Nocedal and Stephen J. Wright. *Numerical Optimization*. Springer, New York, NY, USA, second edition, 2006.

[14] Sergej Rjasanow and Wolfgang Wagner. *Stochastic numerics for the Boltzmann equation*. Springer, 2005.

[15] Ching Shen. *Rarefied gas dynamics: fundamentals, simulations and micro flows*. Springer Science & Business Media, 2006.

[16] Quanhua Sun and Iain D Boyd. Evaluation of macroscopic properties in the direct simulation monte carlo method. *Journal of Thermophysics and Heat Transfer*, 19 (3):329–335, 2005.

[17] Craig White, Matthew K Borg, Thomas J Scanlon, Stephen M Longshaw, B John, DR Emerson, and Jason M Reese. dsmcfoam+: An openfoam based direct simulation monte carlo solver. *Computer Physics Communications*, 224:22–43, 2018.

[18] DJ Whitehouse. Handbook of surface metrology, inst. *Physics Publ., London*, 283, 1994.